Geophysical Journal International

Geophys. J. Int. (2018) **213,** 1244–1262
Advance Access publication 2018 February 1
GJI Marine geosciences and applied geophysics

doi: 10.1093/gji/ggy040

Dynamic seismic signatures of saturated porous rocks containing two orthogonal sets of fractures: theory versus numerical simulations

Junxin Guo,[1] J. Germán Rubino,[2] Stanislav Glubokovskikh[1] and Boris Gurevich[1,3]

[1]*Department of Exploration Geophysics, Curtin University, GPO Box U*1987, *Perth, Western Australia* 6845, *Australia.*
E-mail: junxin.guo@postgrad.curtin.edu.au
[2]*CONICET, Centro Atómico Bariloche - CNEA, San Carlos de Bariloche, Río Negro* 8400, *Argentina*
[3]*CSIRO,* 26 *Dick Perry Avenue, Kensington, Western Australia* 6152, *Australia*

Accepted 2018 January 31. Received 2017 November 2; in original form 2017 May 30

SUMMARY

The dispersion and attenuation of seismic waves are potentially important attributes for the non-invasive detection and characterization of fracture networks. A primary mechanism for these phenomena is wave-induced fluid flow (WIFF), which can take place between fractures and their embedding background (FB-WIFF), as well as within connected fractures (FF-WIFF). In this work, we propose a theoretical approach to quantify seismic dispersion and attenuation related to these two manifestations of WIFF in saturated porous rocks permeated by two orthogonal sets of fractures. The methodology is based on existing theoretical models for rocks with aligned fractures, and we consider three types of fracture geometries, namely, periodic planar fractures, randomly spaced planar fractures and penny-shaped cracks. Synthetic 2-D rock samples with different degrees of fracture intersections are then explored by considering both the proposed theoretical approach and a numerical upscaling procedure that provides the effective seismic properties of generic heterogeneous porous media. The results show that the theoretical predictions are in overall good agreement with the numerical simulations, in terms of both the stiffness coefficients and the anisotropic properties. For the seismic dispersion and attenuation caused by FB-WIFF, the theoretical model for penny-shaped cracks matches the numerical simulations best, whereas for representing the effects due to FF-WIFF the periodic planar fractures model turns out to be the most suitable one. The proposed theoretical approach is easy to apply and is applicable not only to 2-D but also to 3-D fracture systems. Hence, it has the potential to constitute a useful framework for the seismic characterization of fractured reservoirs, especially in the presence of intersecting fractures.

Key words: Fracture and flow; Numerical modelling; Seismic anisotropy; Seismic attenuation; Theoretical seismology.

1 INTRODUCTION

Fractures are important objects in many geological formations, as they provide additional conduits for fluid flow. This implies that their presence can significantly improve the effective permeability of the involved material, especially in the case of low-permeability reservoirs (e.g. Gale *et al*. 2007; Ostojic *et al*. 2012). Furthermore, fractures also have a great influence on the elastic properties of fractured formations. Due to their small aspect ratio, even a small density of fractures can greatly reduce the elastic stiffness of the host formation (e.g. Bristow 1960; Walsh 1965; Kuster & Toksöz 1974; Mavko *et al*. 1995; Glubokovskikh *et al*. 2016). For these reasons, the detection and characterization of fractures are topics of great importance in many disciplines, such as oil/gas exploration and production, carbon geosequestration, nuclear waste disposal, and underground engineering, among many others (e.g. Huo & Gong 2010; Neuzil 2013; Lisjak *et al*. 2014; Yuan *et al*. 2014; Liu *et al*. 2017).

The most direct method for fracture detection and characterization is the study of outcrops or core samples (e.g. Zeeb *et al*. 2013; Basquet *et al.* 2008), which provides first-hand information on the geometries and distribution of the fractures in the formation of interest. However, it can only provide such information for a very limited rock volume. Apart from these kinds of observations, well logging methods are also often applied in the characterization of fracture networks (e.g. Zazoun 2013; Che *et al*. 2015). Detailed information on the fractures present around the borehole can be obtained, especially from imaging data. Nevertheless, these methods also suffer from the limited sampling of the affected rock volume, which is confined to the vicinity of the borehole. Furthermore, the accuracy of

fracture detection and characterization through cores or logs is also influenced by the possible existence of coring- or drilling-induced fractures. For these reasons, non-invasive approaches that can offer fracture information on a larger scale are of significant interest. In this context, the seismic method presents a special value due to its ability to provide, in a non-invasive manner, information on the probed fractured volume on a relatively large scale (e.g. Wang *et al*. 2007; Liu & Martinez 2012).

In most cases, the resolution of the seismic data is insufficient to directly image fractures and, hence, seismic attributes are often used for this purpose (e.g. Bakulin *et al*. 2000a, 2000b, 2000c; Vlastos *et al*. 2007; Sassen & Everett 2009; Gao 2013). In particular, in presence of mesoscopic fractures, seismic waves experience velocity dispersion and attenuation, as well as frequency-dependent anisotropy, which in turn can serve as valuable signatures for fracture detection and characterization (e.g. Chapman 2003; Lambert *et al*. 2006; Rubino *et al*. 2014). An important physical mechanism for the associated energy dissipation is wave-induced fluid flow (WIFF) between the fractures and the background pores (FB-WIFF) (Müller *et al*. 2010). When a seismic wave propagates through a fractured porous rock, due to the typically large contrast between the compressibility of the fractures and that of the background medium, a strong fluid pressure gradient will be induced between these two regions. Hence, oscillatory fluid flow will occur between them, which results in energy dissipation due to viscous friction. Up until now, extensive research has been carried out to explore this mechanism for rocks containing aligned fractures. Chapman (2003) considered fluid flow both on the grain scale (between microcracks and background pores) and fracture scale (between fractures and background pores). The interactions between these two scales are also analysed and the resulting frequency-dependent anisotropy is then investigated. Brajanovski *et al*. (2005) modelled WIFF effects considering a saturated rock with aligned planar fractures as a special case of a periodic layered porous medium. Galvin & Gurevich (2006, 2007, and 2009) studied the case of sparsely and randomly distributed aligned penny-shaped cracks embedded in a saturated porous rock. Gurevich *et al*. (2009) proposed a unified branching function approach to describe the seismic dispersion and attenuation due to the FB-WIFF, which was recently extended by Guo *et al*., 2018a, 2018b) for considering the effects of finite fracture thickness.

In a series of papers, Rubino *et al*. (2013, 2014, and 2017) found that besides FB-WIFF, WIFF also occurs within connected mesoscopic fractures (FF-WIFF), which can have a significant influence on the dispersion, attenuation, and anisotropy of seismic waves. Since this fluid flow critically depends on the connectivity degree of the probed fracture network, these results suggest the possibility to detect fracture connectivity and, hence, to quantify the effective permeability of fractured formations using seismic data. It is then of great importance to further explore this WIFF manifestation. However, to date, this task has been addresses mainly using numerical simulations (Rubino *et al*. 2013, 2014, 2017), and little work has been done to explore the theoretical side of this manifestation of WIFF. A recent effort in this direction was published by Guo *et al*. (2017), who quantified the elastic properties of rocks containing two perpendicular sets of non-intersecting and intersecting fractures. These authors computed the stiffness coefficients in the low- and high-frequency limits as well as at an intermediate frequency range for which fractures are hydraulically isolated from the background but full pressure communication within connected fractures occurs. In addition, the characteristic frequencies separating the different frequency regimes were also derived. The work of Guo *et al*. (2017) therefore provides the basis to further develop a theoretical framework that allows to quantify seismic dispersion and attenuation incorporating the effects of both FB- and FF-WIFF. In this paper, we complement and extend the theoretical predictions of Guo *et al*. (2017) to the full frequency range. The resulting effective properties are then compared with corresponding numerical simulations.

2 THEORY

2.1 Unified theoretical model for the *P*-wave modulus in the direction perpendicular to the fracture plane for rocks with aligned fractures

Despite the complex geometrical properties of fractures, for simplicity they are usually approximated as planar fractures or penny-shaped cracks. If the radii of the fractures are much larger than the predominant seismic wavelength and the fracture spacing (e.g. large joints), fractures can be treated as planes of weakness, which are also called planar fractures (Schoenberg 1980; Gurevich *et al*. 2009). In this case, fractures can be modelled as thin and highly porous layers, and the corresponding fractured rock can be treated as a layered porous medium (Brajanovski *et al*. 2005). In this context, it is important to remark that this poroelastic representation of fractures is consistent with the fact that natural fractures tend to be 'rough-walled', with the walls being in contact with each other at certain locations and often containing rock fragments, weathering products, or mineral deposits in the regions between the contact areas. When a seismic wave propagates through such a medium, seismic dispersion and attenuation occurs due to FB-WIFF. If the planar fractures are distributed periodically in an isotropic porous background, the frequency-dependent and complex-valued saturated *P*-wave modulus in the direction perpendicular to the fracture plane can be obtained theoretically (Brajanovski *et al*. 2005).

On the other hand, if the fracture radii are much smaller than the fracture spacing but much larger than the pore sizes, the fractures are then often modelled as penny-shaped cracks, that is, strongly oblate spheroids. For saturated porous rocks with aligned penny-shaped cracks, FB-WIFF will also occur in response to the propagation of a seismic wave. If the aligned penny-shaped cracks are distributed randomly and sparsely in an isotropic porous background medium, the complex-valued and frequency-dependent saturated *P*-wave modulus in the direction perpendicular to the fracture plane can be obtained by solving a mixed boundary value problem in the context of Biot's equations of poroelasticity (Galvin & Gurevich, 2006, 2007, 2009).

In order to obtain a unified model, Gurevich *et al*. (2009) applied a branching function approach (Johnson 2001; Pride & Berryman 2003) to express the *P*-wave modulus of a saturated porous rocks with aligned fractures in the direction perpendicular to the fracture plane. The resulting frequency-dependent and complex-valued saturated *P*-wave modulus c^{sat} satisfies:

$$\frac{1}{c^{\text{sat}}} = \frac{1}{C_1}\left[1 + \left(\frac{C_1 - C_0}{C_0}\right) / \left(1 - \varsigma + \varsigma\sqrt{1 - i\frac{\omega\tau}{\varsigma^2}}\right)\right], \qquad (1)$$

where ω is the seismic wave angular frequency; ζ and τ are parameters that shape the *P*-wave dispersion and attenuation curves as functions of frequency; and C_0 and C_1 represent the values of the *P*-wave modulus in the low- and high-frequency limits, respectively.

The low- and high-frequency asymptotes of eq. (1) can be expressed as

$$\frac{1}{c^{\mathrm{sat}}} = \frac{1}{C_0}\left(1 + i\omega T\right), \omega\tau << \varsigma^2, \tag{2}$$

$$\frac{1}{c^{sat}} = \frac{1}{C_1}\left(1 + \frac{G}{\sqrt{-i\omega}}\right), \omega\tau >> 1. \tag{3}$$

Hence, the parameters T and G control the behaviours of the P-wave modulus at low and high frequencies, respectively. The shape parameters ζ and τ can be related to the parameters T and G as follows:

$$\tau = \left(\frac{C_1 - C_0}{C_0 G}\right)^2, \tag{4}$$

$$\varsigma = \frac{(C_1 - C_0)^3}{2C_1 C_0^2 T G^2}. \tag{5}$$

Thus, the frequency-dependent saturated P-wave modulus in the direction perpendicular to the fracture plane can be computed if the values of T and G are obtained. Gurevich *et al*. (2009) derived expressions for these parameters for the case with infinitesimal fracture thickness. Recently, Guo *et al*. (2018a) showed that the influence of the finite fracture thickness on the P-wave modulus can be significant, and obtained corresponding expressions for T and G for both planar fractures and penny-shaped cracks.

For planar fractures with finite thickness, when they are distributed periodically in an isotropic porous background medium, the saturated P-wave modulus of the fractured rock in the direction perpendicular to the fracture plane can be obtained as follows (e.g. Brajanovski *et al*. 2005):

$$\frac{1}{c^{\mathrm{sat}}} = \frac{1}{C_1} + \frac{2}{\sqrt{i\omega\eta}H} \times \frac{\left(\frac{\alpha_b M_b}{C_b} - \frac{\alpha_c M_c}{C_c}\right)^2}{\sqrt{\frac{M_b L_b}{C_b \kappa_b}}\cot\left(\sqrt{\frac{i\omega\eta C_b}{\kappa_b M_b L_b}}\frac{f_b H}{2}\right) + \sqrt{\frac{M_c L_c}{C_c \kappa_c}}\cot\left(\sqrt{\frac{i\omega\eta C_c}{\kappa_c M_c L_c}}\frac{f_c H}{2}\right)}, \tag{6}$$

where C_b and L_b are the P-wave moduli of the saturated and dry background, respectively; κ_b is the permeability of the background; f_b is the fraction of background with respect to the whole porous medium; $\alpha_b = 1 - K_b/K_g$ is the Biot's coefficient of the background, with K_b being the bulk modulus of the dry background and K_g that of the solid grains; and $M_b = K_g/[(1 - K_b/K_g) - \phi_{bg}(1 - K_g/K_f)]$ is the Biot's modulus of the background, with K_f being the fluid bulk modulus and ϕ_{bg} the porosity of the background. The subscript c represents the corresponding values for the porous material infilling the fractures. In addition, H represents the distance between consecutive fractures, and $S_1 = 1/H$ is the specific fracture surface area per unit volume for the planar fractures. Both the fractures and the background pores are saturated with the same fluid with shear viscosity η.

At low frequencies, we can obtain the asymptote of eq. (6) as follows:

$$\frac{1}{c^{\mathrm{sat}}} = \frac{1}{C_0}\left[1 + i\omega\frac{1}{12}\frac{C_1 - C_0}{C_1}\frac{\left(\frac{f_b}{\kappa_b} + \frac{f_c}{\kappa_c}\right)\eta H^2}{\frac{M_b L_b}{C_b f_b} + \frac{M_c L_c}{C_c f_c}}\right]. \tag{7}$$

Comparing eq. (7) with eq. (2) gives the expression of T for the periodic planar fracture case as follows:

$$T = \frac{1}{12}\frac{C_1 - C_0}{C_1}\frac{\left(\frac{f_b}{\kappa_b} + \frac{f_c}{\kappa_c}\right)\eta H^2}{\frac{M_b L_b}{C_b f_b} + \frac{M_c L_c}{C_c f_c}}. \tag{8}$$

At high frequencies, the asymptote of eq. (6) is as follows:

$$\frac{1}{c^{\mathrm{sat}}} = \frac{1}{C_1}\left[1 + \frac{1}{\sqrt{-i\omega}}\frac{2C_1\left(\frac{\alpha_b M_b}{C_b} - \frac{\alpha_c M_c}{C_c}\right)^2}{H\left(\sqrt{\frac{M_b L_b \eta}{C_b \kappa_b}} + \sqrt{\frac{M_c L_c \eta}{C_c \kappa_c}}\right)}\right]. \tag{9}$$

Comparison of eq. (9) with eq. (3) gives the expression of G for the periodic planar fracture case as follows:

$$G = \frac{2S_1 C_1\left(\frac{\alpha_b M_b}{C_b} - \frac{\alpha_c M_c}{C_c}\right)^2}{\sqrt{\frac{M_b L_b \eta}{C_b \kappa_b}} + \sqrt{\frac{M_c L_c \eta}{C_c \kappa_c}}}. \tag{10}$$

If the planar fractures are distributed randomly, as the fluid diffusion length gets very small values at high frequencies, the energy only dissipates in the immediate vicinity of the fracture surface. Hence, the seismic dispersion and attenuation at high frequencies are independent of the characteristics of the probed fracture distribution. This means that the expression of G for the random planar fracture case is the same as that for the periodic planar fracture case (eq. 10). However, at low frequencies, due to the large fluid pressure diffusion lengths, seismic dispersion and attenuation will be affected by the characteristics of the fracture distribution. As the effective fracture spacing will tend to infinity for the random planar fracture distribution case (e.g. Gurevich *et al*. 2009), the corresponding value of T will then also tend to infinity.

For penny-shaped cracks with finite thickness, Galvin & Gurevich (2009) showed that the effects of finite fracture thickness are negligible at low frequencies. Hence, we can use the same expression for T for the penny-shaped cracks with finite thickness as that for infinitesimal thickness case. This expression was given by Gurevich *et al*. (2009), which reads

$$T = \frac{2(C_b - \alpha_b M_b)^2\left(2 - 4\alpha_b g_b + 3\alpha_b^2 g_b^2\right)a^2\varepsilon\eta}{15\mu_b g_b(1 - g_b)^2 C_b L_b \kappa_b}, \tag{11}$$

where μ_b is the dry background shear modulus and g_b is the ratio of μ_b to L_b; a is the radius of the penny-shaped cracks; $\varepsilon = 3f_c/(4\pi\beta)$ is the crack density with β being the crack aspect ratio. Substituting the relation between the P-wave moduli of the saturated fractured rock in the low- and high-frequency limits (Gurevich *et al*. 2009), eq. (11) can be rewritten as

$$T = \frac{1}{5}\frac{C_1 - C_0}{C_0}\frac{\left(2 - 4\alpha_b g_b + 3\alpha_b^2 g_b^2\right)a^2\eta}{g_b\left(1 - g_b\right)L_b\kappa_b}. \tag{12}$$

At high frequencies, it is difficult to derive an analytical expression for G corresponding to a porous rock containing penny-shaped cracks with finite thickness. However, we can obtain an approximate expression by comparing with the planar fracture case. Due to the small values that the fluid diffusion length gets at high frequencies, energy dissipation only occurs at the immediate vicinity of the fracture surfaces. This implies that the energy dissipation depends critically on the fracture surface area for both the planar fracture and penny-shaped crack cases. Gurevich *et al*. (2009) showed that the expression for G for the planar fracture and penny-shaped crack cases has the same form when the fracture thickness is infinitesimal,

except that the specific surface areas for these two types of fractures are different. Hence, for the case with finite fracture thickness considered in this work, we also assume that the expression of G for the penny-shaped crack case has the same form as that for the planar fracture case. However, apart from correcting for the specific surface area, it has to be taken into account that the physical properties of the fractures are explicitly involved in the expression of G for fractures with finite thickness (eq. 10). To take into account the effects due to the different geometrical characteristics of the penny-shaped cracks with respect to planar fractures, and considering that the amount of energy dissipation is controlled by the mechanical contrast between fractures and background, we employ an equivalent infill material when using eq. (10) for computing the value of G for rocks containing penny-shaped cracks with finite thickness

$$G = \frac{2S_2C_1\left(\frac{\alpha_b M_b}{C_b} - \frac{\alpha_{ce} M_{ce}}{C_{ce}}\right)^2}{\sqrt{\frac{M_b L_b \eta}{C_b \kappa_b}} + \sqrt{\frac{M_{ce} L_{ce} \eta}{C_{ce} \kappa_{ce}}}}, \tag{13}$$

where $S_2 = \pi\varepsilon/a$ is the specific fracture surface area per unit volume for the penny-shaped cracks, and the subscript 'ce' represents the properties of the equivalent infill material. The equivalent material has the same porosity and permeability as that for the infill material of the penny-shaped cracks. However, the effective dry frame P-wave and shear moduli, L_{ce} and μ_{ce}, are calculated as follows (Brajanovski *et al*. 2005; Guo *et al*. 2018a):

$$L_{ce} = \frac{f_c}{Z_N}, \tag{14}$$

$$\mu_{ce} = \frac{f_c}{Z_T}, \tag{15}$$

with Z_N and Z_T being the normal and tangential excess compliances of the dry penny-shaped cracks, respectively; and f_c being the fraction of the penny-shaped cracks in the rock. Eqs (14) and (15) ensure that the excess compliances of the dry rock considering planar fractures containing the equivalent infill material are the same as those of the same rock containing penny-shaped cracks. The other effective elastic properties of the equivalent infill material can be calculated from L_{ce} and μ_{ce}. The values of G provided by eq. (13) are in good agreement with corresponding numerical simulations (Guo *et al*. 2018a).

More details with respect to the derivation of T and G for rocks having aligned planar fractures or penny-shaped cracks of finite thickness can be found in Guo *et al*. (2018a).

2.2 Extension to the case of rocks having two perpendicular sets of fractures

To study the effects of fracture intersections on seismic dispersion and attenuation, we consider a simple case consisting of a rock with two sets of perpendicular fractures, having all the fractures the same geometrical characteristics. We assume that the two fracture sets are perpendicular to the x- and y-axes, respectively, and we take into account the presence of intersecting and non-intersecting fracture networks, such as those shown in Fig. 1.

2.2.1 Non-intersecting fracture case

For rocks with two orthogonal sets of non-intersecting fractures, a P-wave propagating perpendicular to one of the fracture sets will induce oscillatory fluid flow between such fractures and the background pores (FB-WIFF). The fractures parallel to the propagation direction, on the other hand, are not expected to affect significantly the behaviour of the seismic wave (Rubino *et al*. 2014). Hence, the two P-wave moduli in the directions perpendicular to the two fracture sets, c_{11} and c_{22}, can be directly obtained in a similar way as for rocks with aligned fractures (eq. 1). That is, the expressions for T and G for the cases with orthogonal non-intersecting planar fractures as well as for non-intersecting penny-shaped cracks can be calculated using the same formulas as for the corresponding aligned fracture case. As the fractures considered here have the same geometrical characteristics, at least one of the non-intersecting fracture sets will have the fracture spacing that is larger than the fracture radii under the periodical distributions. This violates the definition of planar fractures. Hence, the non-intersecting periodic planar fracture case is not realizable and we only consider the randomly spaced planar fracture and penny-shaped crack cases here. For randomly-spaced planar fractures, T tends to infinity and G can be calculated using eq. (8). For penny-shaped cracks, T and G can be calculated using eqs (12) and (13), respectively. However, it should be noted that, for calculating c_{11}, the properties of the aligned fracture set in these equations correspond to those of the fracture set perpendicular to the x-axis, whereas for calculating c_{22} the properties of the fracture set perpendicular to the y-axis should be used. Furthermore, the P-wave moduli in the low- and high- frequency limits C_0 and C_1 need to be replaced by the corresponding values of c_{11} or c_{22}.

It is important to remark here that, due to Poisson ratio effects, a small amount of fluid flow also occurs between the fracture set parallel to the wave propagation direction and the background pores. The corresponding effects on the P-wave moduli are expected to be negligible and, therefore, are not accounted for in the approach proposed here. This is in agreement with the results of Rubino *et al*. (2014) and is supported by the numerical analysis considered in this work.

2.2.2 Intersecting fracture case

In the case of rocks with two perpendicular sets of intersecting fractures, a P-wave propagating perpendicular to one of the fracture sets will not only induce FB-WIFF, but also FF-WIFF. Hence, the P-wave modulus in the direction perpendicular to one fracture set will experience two stages of dispersion and attenuation, which are due to these two manifestations of WIFF. The characteristic frequencies for these two stages of dispersion and attenuation are proportional to the permeability of the background medium and that of the material composing the fractures, respectively (Guo *et al*. 2017). Consequently, since typically the permeability of the background medium is much lower than that of the fractures, the dispersion and attenuation due to FB-WIFF occur at much lower frequencies than in the case of FF-WIFF.

To obtain the frequency-dependent P-wave moduli c_{11} and c_{22} for the first stage of dispersion and attenuation (FB-WIFF), the corresponding expressions for T and G are needed. For rocks with two orthogonal sets of fractures having the same geometries, when a P-wave propagates perpendicular to one of the fracture sets, the resulting FB-WIFF is expected to be primarily controlled by the stiffness contrast between such fracture set and the background medium. Hence, it is reasonable to approximate the expressions for T and G using the same form as those for aligned fracture case [eqs (8) and (10) for planar fractures, and —(13) for penny-shaped cracks]. However, even in the high frequency limit of FB-WIFF, connected

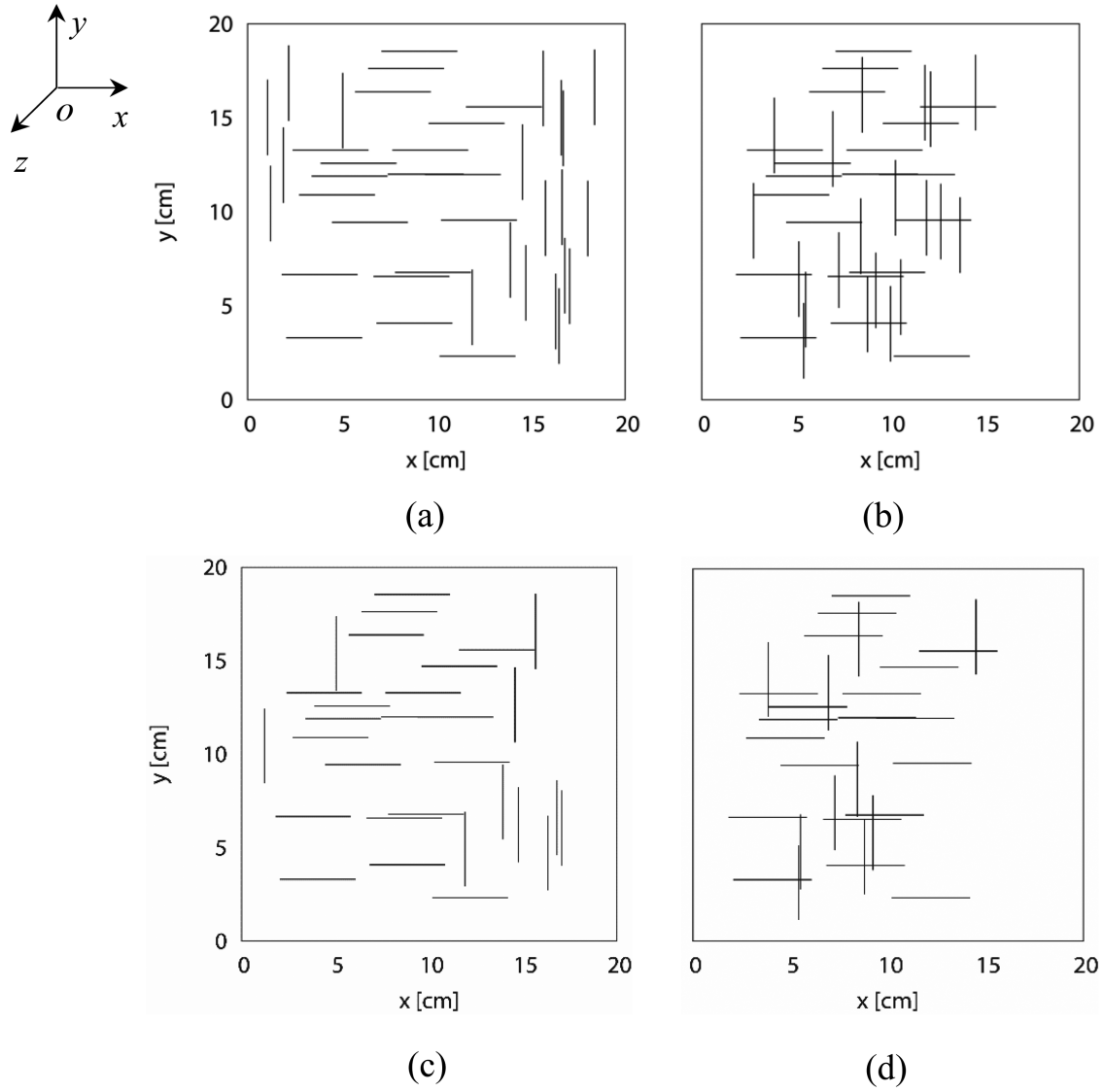

Figure 1. Geometries of the investigated 2-D synthetic rock samples. Samples (a) and (b) have 20 horizontal and 20 vertical fractures, whereas samples (c) and (d) also have 20 horizontal fractures but 10 vertical fractures. In addition, while samples (a) and (c) contain non-intersecting fractures, in samples (b) and (d) all vertical fractures have at least one intersection.

fractures will be in pressure communication with each other, and hence, the system will be softer than in the case of only one set of aligned fractures. This implies that the dispersion and attenuation due to FB-WIFF will also be weaker in presence of connected fractures, as shown by Rubino *et al*. (2014). As the dispersion and attenuation at low and high frequencies are controlled by the parameters T and G, respectively (eqs 2 and 3), weaker dispersion and attenuation means smaller values of T and G for the intersecting fracture case in comparison with the aligned fracture case. Hence, the values of T and G need to be scaled down here. Since the amplitude of the dispersion and attenuation are dominated by the elastic properties in the low- and high-frequency limits (Mavko *et al*. 2009), the scaled values of T and G can be easily obtained by replacing the P-wave moduli in the low- and high-frequency limits C_0 and C_1 in eqs (8), (10), (12) and (13) with the corresponding limiting values of c_{11} or c_{22} due to FB-WIFF for the intersecting fracture case. It should be noted that T for the randomly spaced planar fracture case still tends to infinity (corresponding to the zero value of ζ). Similar to the non-intersecting fracture case, the parameters of the fracture set perpendicular to the x-axis should be used when calculating T and G for c_{11}, whereas those of the other fracture set for computing c_{22}. In the numerical examples, we will see that the theoretical predictions using the scaled values of T and G are in good agreement with the numerical simulations.

For computing the P-wave moduli c_{11} and c_{22} for the second stage of dispersion and attenuation (FF-WIFF), it is important to take into account that if the frequency of the propagating wave is above the high-frequency limit of FB-WIFF, the fluid in the fractures does not have enough time to communicate with that of the background and, therefore, the fractures are hydraulically isolated. However, the fluid can still communicate between connected fractures. Hence, if a P-wave propagates perpendicular to one of the fracture sets, the fluid from such fractures will be injected into (or withdrawn from) the connected ones during the compression (or extension) cycle. This indicates that the fluid in the fracture set perpendicular to the wave propagation direction is communicating with an effective medium, for which the other fracture set acts as the porosity and the saturated background medium acts as the solid phase. This implies that this

process can be represented by aligned fractures embedded in an effective medium and, again as before, the eqs (8), (10), (12) and (13) can be used to compute the required parameters T and G. In order to do so, the properties of the effective medium are needed. The elastic properties of the dry effective medium are obtained by adding the dry fractures into the saturated background medium using the linear slip theory (Schoenberg & Sayers 1995; Guo *et al*. 2017). The saturated elastic properties of this effective medium are then obtained by using the anisotropic Gassmann's equation (Gurevich 2003; Guo *et al*. 2017). Furthermore, the permeability of the effective medium along x-axis (or y-axis) κ_e can be obtained based on the definition of permeability:

$$\kappa_e = \kappa_c \phi_e, \tag{16}$$

where κ_c is the permeability of the material composing the fracture set parallel to x- or y- axis, and ϕ_e is the volume fraction that the corresponding fracture set occupies.

With the properties of the effective medium and the fracture sets, the expressions of T and G for c_{11} and c_{22} for the second stage of dispersion and attenuation can be calculated through eqs (8), (10), (12) and (13) by replacing the properties of the background medium with those of the effective medium and the properties of the aligned fractures with those of the fracture set perpendicular to the x- and y-axes, respectively. Also, we need to replace the elastic properties in the low- and high-frequency limits C_0 and C_1 with the corresponding values for the stage of dispersion and attenuation due to FF-WIFF. It should be noted that T for randomly spaced planar fractures still tends to infinity here.

It is important to remark here that, different from the case of an isotropic background, the effective medium is anisotropic. Hence, strictly speaking, the expressions for T and G should be derived for fractures in an anisotropic background. However, the resulting equations may get very complicated. To keep our approach easy to apply, we still use eqs (8), (10), (12) and (13) to calculate T and G. However, the background porosity in these equations is replaced by the fraction that the fracture set along x-axis occupies in the rock for c_{11} and that occupied by the fracture set along y-axis for c_{22}. And also, the background permeability and elastic properties are replaced by those of the effective medium along x-axis for c_{11} and those along y-axis for c_{22}. This may cause some errors, which we will discuss in the numerical example section of this work. In addition, in our current approach, we assume that all the fractures are connected to at least one orthogonal fracture and, hence, the fluid pressure increase induced by the seismic wave can be released. If there are isolated fractures, the rock will behave in a stiffer manner due to the unreleased fluid pressure. This will also be analysed in the numerical example section.

2.3 Elastic properties in the low- and high-frequency limits for the two manifestations of WIFF

To determine seismic dispersion and attenuation from eq. (1), the elastic properties in the low- and high-frequency limits for each manifestation of WIFF are needed. For rocks with non-intersecting fractures, only FB-WIFF occurs. Hence, we only need to obtain the elastic properties in the low- and high- frequency limits for this WIFF manifestation in this case. In the low-frequency limit, the fluid in the fractures has enough time to communicate with that in the background pores, and therefore, the fluid pressure is uniform throughout the rock. Under this condition, we can first add the dry fractures into the dry background medium using the linear slip theory (Schoenberg & Sayers 1995) to obtain the elastic properties of the dry fractured rock. The elastic properties of the saturated fractured rock can then be calculated by using the anisotropic Gassmann's equation (Gurevich 2003). Conversely, in the high-frequency limit, the fluid in the fractures does not have enough time to communicate with that in the background pores. Hence, the fractures are hydraulically isolated from the saturated background medium. In this case, we first obtain the compliances of the hydraulically isolated fractures from the dry fracture compliances using a theory for isolated fluid-filled fractures (Hudson 1981; Schoenberg & Douma 1988; Gurevich 2003). Then, the elastic properties of the saturated fractured rock can be obtained by adding the hydraulically isolated fractures into the saturated background medium using the linear slip theory, with the elastic properties of the saturated background calculated by using the isotropic Gassmann's equation (Guo *et al*. 2017).

For rocks with intersecting fractures, apart from FB-WIFF, FF-WIFF can also occur. For the FB-WIFF, the elastic properties in its low-frequency limit can be obtained by using the linear slip theory and the anisotropic Gassmann's equation since the fluid pressure is uniform throughout the rocks. This procedure is similar to that for the non-intersecting fracture case. On the contrary, in its high-frequency limit, the fluid in the fractures does not have enough time to communicate with that of the background pores due to its low permeability. However, as the permeability of the fractures is much higher than that of the background, the fluid can still communicate within connected fractures. Hence, the fluid pressure will be uniform inside the system of connected fractures, but with a value different from that of the saturated background medium. Under this condition, we can obtain the elastic properties of the saturated fractured rock by first adding the dry fractures into the saturated background medium using the linear slip theory. Then, the dry fractures can be saturated using the anisotropic Gassmann's equation, with the saturated background medium acting as the solid phase and the fracture porosity acting as the porosity (Guo *et al*. 2017). For FF-WIFF, the elastic properties in its low-frequency limit coincide with those in the high-frequency limit of FB-WIFF. However, in the high-frequency limit of the FF-WIFF, the fractures will be hydraulically isolated from both the background medium and the other fractures. Hence, similar to the non-intersecting fracture case, we can calculate the corresponding elastic properties by adding the hydraulically isolated fractures into the saturated background medium using the linear slip theory.

The reader is referred to the work of Guo *et al*. (2017) for the details on the determination of the elastic properties in the low- and high-frequency limits for the two manifestations of WIFF.

2.4 Full stiffness coefficients

With the values of T and G obtained for the P-wave moduli in the directions along the x- and y-axes (c_{11} and c_{22}), and the corresponding elastic properties in the low- and high-frequency limits, the frequency-dependent P-wave moduli c_{11} and c_{22} can be calculated. For rocks with non-intersecting fractures, c_{11} and c_{22} can be written as follows:

$$\frac{1}{c_{ii}} = \frac{1}{c_{ii}^{hf}}\left[1 + \left(\frac{c_{ii}^{hf} - c_{ii}^{lf}}{c_{ii}^{lf}}\right) \Big/ \left(1 - \varsigma_i + \varsigma_i \sqrt{1 - i\frac{\omega\tau_i}{\varsigma_i^2}}\right)\right], \quad i = 1, 2 \tag{17}$$

where c_{ii}^{lf} and c_{ii}^{hf} are the corresponding P-wave moduli in the low- and high- frequency limits, respectively; and ζ_i and τ_i are the shape

parameters for c_{ii}, which can be calculated from T_i, G_i, c_{ii}^{lf}, and c_{ii}^{hf} using eqs (4) and (5).

For rocks with intersecting fractures, there are two stages of seismic dispersion and attenuation which are due to the FB- and FF-WIFF. For each stage, we can calculate the frequency-dependent *P*-wave moduli c_{11} and c_{22} through the use of eq. (17), with the involved parameters evaluated for the considered WIFF manifestation. We can then combine these two stages of seismic dispersion and attenuation as follows:

$$\frac{1}{c_{ii}} = \frac{1}{c_{ii}^{hf\_2}}\left\{1+\left[\frac{c_{ii}^{hf\_2}-c_{ii}^{1}(\omega)}{c_{ii}^{1}(\omega)}\right]\Big/\left(1-\varsigma_{2i}+\varsigma_{2i}\sqrt{1-i\frac{\omega\tau_{2i}}{\varsigma_{2i}^{2}}}\right)\right\}, \quad i=1,2 \tag{18}$$

where $c_{ii}^{hf_2}$is the *P*-wave moduli along *x*- or *y*- axis in the high-frequency limit for the second stage of seismic dispersion and attenuation (due to FF-WIFF) and ζ_{2i} and τ_{2i} are the corresponding shape parameters; and $c_{ii}^{1}(\omega)$ is the frequency-dependent *P*-wave moduli calculated from eq. (17) for the first stage of seismic dispersion and attenuation (due to FB-WIFF).

Hence, we have obtained the frequency-dependent *P*-wave moduli c_{11} and c_{22} for both rocks with non-intersecting and intersecting fractures. For the other stiffness coefficients, we can also obtain their frequency-dependent values from eqs (17) and (18). Following Gurevich *et al*. (2009), for all the stiffness coefficients, each stage of dispersion and attenuation (due to FF- or FB-WIFF) is expected to be controlled by two crossover frequencies:

$$\omega_P = \frac{2\varsigma^2}{\tau}, \tag{19}$$

$$\omega_M = \frac{C_1}{C_0}\frac{1}{\tau}. \tag{20}$$

These two crossover frequencies separate each stage of dispersion and attenuation in three regimes where the seismic velocities and attenuation, or stiffness coefficient, vary with frequency in a different manner.

Numerical simulations (Guo *et al*. 2017) show that all the stiffness coefficients have similar frequency-dependent behaviours for samples with relatively high symmetry (equal number of horizontal and vertical fractures). As discussed by Guo *et al*. (2017), the characteristic frequency for FB-WIFF is controlled by the fracture geometries and the properties of the background medium, whereas that for FF-WIFF is determined by the fracture geometries and the properties of an effective background medium. Hence, for samples with relatively low symmetry, the crossover frequencies for FB-WIFF for all the stiffness coefficients should still be similar as both the properties of the background medium and the fracture geometries do not change with the incidence angle of the seismic wave. However, for FF-WIFF, while the fracture geometries remain unchanged with the wave incidence angle, the properties of the effective background medium can vary. This may result in some shifts of the corresponding crossover frequencies for different stiffness coefficients. Nevertheless, since we consider fractures having identical shapes and physical properties, these frequency shifts should be rather small unless the number of horizontal and vertical fractures are drastically different. Hence, for the general case, ω_P and ω_M for c_{11} and c_{22} for a given stage of dispersion and attenuation (FB- or FF-WIFF) are expected to be similar, and close to the crossover frequencies of the remaining stiffness coefficients. Based on this fact, the shape parameters for the other stiffness coefficients can be obtained as follows:

$$\tau' = \frac{C_0}{C_0'}\frac{C_1'}{C_1}\tau, \tag{21}$$

$$\zeta' = \sqrt{\frac{\tau'}{\tau}}\zeta, \tag{22}$$

where, for the first or second stage of dispersion and attenuation, τ and ζ are the shape parameters for c_{11} or c_{22} with C_0 and C_1being the values of c_{11} or c_{22} in the low- and high- frequency limits respectively, and τ ', ζ ', C_0' and C_1' are the corresponding values for a different stiffness coefficient of interest.

Using the thus obtained shape parameters τ ' and ζ ' and also the elastic properties in the low- and high-frequency limits for each stage of dispersion and attenuation (Section 2.3), the frequency-dependent values of the other stiffness coefficient can be obtained from eq. (17) for the non-intersecting fracture case and from eq. (18) for the intersecting fracture case. It should be noted here that the τ ' and ζ ' can be estimated from either c_{11} or c_{22} using eqs (21) and (22), as the resulting values are expected to be close. Here, we use the average values of τ ' and ζ ' obtained from both c_{11} and c_{22}.

2.5 Seismic wave velocity and attenuation as functions of incidence angle and associated anisotropic parameters

Once the full stiffness coefficients are computed, we can calculate the seismic wave velocity and attenuation as functions of incidence angle. Guo *et al*. (2017) show that the effective elastic properties of saturated rocks containing two sets of orthogonal fractures correspond to those of an orthorhombic medium. Hence, the complex velocities of the *qP*-, *qSV*-, and *SH*-waves can be calculated from the stiffness coefficients using the formulas for orthorhombic media. The complex velocities in the *x*–*y* plane can then be calculated as follows (Mavko *et al*. 2009):

$$\tilde{V}_{qP} = \left(c_{66}+c_{22}\cos^2\theta+c_{11}\sin^2\theta + \sqrt{\left(c_{66}+c_{22}\cos^2\theta+c_{11}\sin^2\theta\right)^2-4M}\right)^{1/2}(2\rho)^{-1/2}, \tag{23}$$

$$\tilde{V}_{qSV} = \left(c_{66}+c_{22}\cos^2\theta+c_{11}\sin^2\theta - \sqrt{\left(c_{66}+c_{22}\cos^2\theta+c_{11}\sin^2\theta\right)^2-4M}\right)^{1/2}(2\rho)^{-1/2}, \tag{24}$$

$$\tilde{V}_{SH} = \left(\frac{c_{55}\sin^2\theta+c_{44}\cos^2\theta}{\rho}\right)^{1/2}, \tag{25}$$

where ρ is the density of the saturated fractured rock, θ is the incidence angle measured with respect to the *y*-axis, and the expression for *M* is as follows:

$$M = \left(c_{66}\cos^2\theta+c_{11}\sin^2\theta\right)\left(c_{22}\cos^2\theta+c_{66}\sin^2\theta\right) - \left(c_{12}+c_{66}\right)^2\sin^2\theta\cos^2\theta. \tag{26}$$

The complex velocities for seismic waves propagating in the *x*–*z* and *y*–*z* planes can be calculated in a similar way, as can be seen in Mavko *et al*. (2009). After obtaining the complex velocities, the corresponding phase velocities and attenuations for the *qP*-, *qSV*-, and *SH*-waves can be computed as follows (e.g. Carcione *et al*.

2013):

$$V = \left[\mathrm{Re}\left(\frac{1}{\tilde{V}}\right)\right]^{-1}, \tag{27}$$

$$\frac{1}{Q} = \left|\frac{\mathrm{Im}\left(\tilde{V}^2\right)}{\mathrm{Re}\left(\tilde{V}^2\right)}\right|, \tag{28}$$

where $\tilde{V}$ represents the complex velocities of either *qP*-, *qSV*-, or *SH*-waves, and V and $1/Q$ are the corresponding phase velocities and attenuations.

To study the anisotropic properties of fractured rocks, it is convenient to plot Thomsen's style anisotropic parameters. For orthorhombic media, the velocity anisotropic parameters in the x–y plane can be computed as follows (Tsvankin 1997; Collet *et al.* 2014):

$$\varepsilon^{(3)} = \frac{\mathrm{Re}\left(c_{22} - c_{11}\right)}{2\mathrm{Re}\left(c_{11}\right)}, \tag{29}$$

$$\delta^{(3)} = \frac{\left[\mathrm{Re}\left(c_{12} + c_{66}\right)\right]^2 - \left[\mathrm{Re}\left(c_{11} - c_{66}\right)\right]^2}{2\mathrm{Re}\left(c_{11}\right)\mathrm{Re}\left(c_{11} - c_{66}\right)}, \tag{30}$$

$$\gamma^{(3)} = \frac{\mathrm{Re}\left(C_{44} - C_{55}\right)}{2\mathrm{Re}\left(C_{55}\right)}. \tag{31}$$

The velocity anisotropic parameters in the other planes (x-z and y-z planes) can be calculated in a similar way (Tsvankin 1997; Collet *et al.* 2014).

3 NUMERICAL EXAMPLES

3.1 Sample parameters

Following Rubino *et al.* (2014) and Guo *et al.* (2017), we consider 2-D synthetic square samples of side length 20 cm containing 2 orthogonal sets of fractures (Fig. 1), which are representative of different geological formations of interest. The samples shown in Figs 1(a) and (b) contain 20 horizontal and 20 vertical fractures. The major difference between them is that the two perpendicular fracture sets are non-intersecting for one sample, but mostly intersecting for the other one. On the other hand, the samples included in Figs 1(c) and (d) also have 20 horizontal fractures and are characterized by contrasting degrees of fracture connectivity, but they only have 10 vertical fractures.

The coordinate system for the samples is established in Fig. 1, such that the x-axis is along the horizontal direction and the y-axis is along the vertical direction. The z-axis is perpendicular to the x–y plane and the samples are long enough along this direction to ensure that they satisfy the plane strain condition. The properties of the fractures and backgrounds, which remain unchanged for all the samples considered in the analyses, were presented by Guo *et al.* (2017) and we repeat them here for the convenience of readers. For the background we consider a porosity of 0.1 and, for the solid grains, we use a bulk modulus of 37 GPa and a density of 2.65 g cm^{-3}. In addition, the dry bulk and shear moduli for this region are 26 GPa and 31 GPa, respectively, whereas its permeability is 10^{-4} mD. The fractures, on the other hand, have a rectangular geometry with a constant length of ∼4 cm and a thickness of 0.06 cm. We represent them with a highly compliant porous material having a porosity of 0.8 and a permeability of 100 D. The solid grains composing this porous infill material have the same properties as those of the background medium, whereas the dry bulk and shear moduli are 0.04 and 0.02 GPa, respectively (Nakagawa & Schoenberg 2007; Rubino *et al.* 2014). Both the background medium and the fractures are assumed to be fully saturated with water, with a bulk modulus of 2.25 GPa, a shear viscosity of 0.001 Pa s, and a density of 1.09 g cm^{-3}.

Apart from obtaining the stiffness coefficients for the described samples using the theoretical approach presented in this work, for comparison we also compute these parameters employing a numerical upscaling procedure (Rubino *et al.* 2016). To do so, three numerical oscillatory relaxation tests are applied on a given sample of interest, and the responses are obtained by solving the Biot's (1941) quasi-static poroelastic equations. The volume average responses of the probed sample allow us to define an equivalent anisotropic viscoelastic solid which, in turn, provide us with the stiffness coefficients of interest. This numerical approach is briefly outlined in Appendix.

To predict the frequency-dependent stiffness coefficients theoretically, we need to calculate the dry fracture compliance matrixes for the fracture sets perpendicular to the x-axis ($\mathbf{S}_{c1}$) and y- axis ($\mathbf{S}_{c2}$):

$$\mathbf{S}_{c1} = \begin{pmatrix} Z_{N1} & 0 & 0 & 0 & 0 & 0 \\ 0 & 0 & 0 & 0 & 0 & 0 \\ 0 & 0 & 0 & 0 & 0 & 0 \\ 0 & 0 & 0 & 0 & 0 & 0 \\ 0 & 0 & 0 & 0 & Z_{T3} & 0 \\ 0 & 0 & 0 & 0 & 0 & Z_{T1} \end{pmatrix}, \tag{32}$$

$$\mathbf{S}_{c2} = \begin{pmatrix} 0 & 0 & 0 & 0 & 0 & 0 \\ 0 & Z_{N2} & 0 & 0 & 0 & 0 \\ 0 & 0 & 0 & 0 & 0 & 0 \\ 0 & 0 & 0 & Z_{T4} & 0 & 0 \\ 0 & 0 & 0 & 0 & 0 & 0 \\ 0 & 0 & 0 & 0 & 0 & Z_{T2} \end{pmatrix}. \tag{33}$$

Here, each fracture set has two different tangential fracture compliances due to the fact that the fracture lengths along x- and z-axes are different for our 2-D samples (Far *et al.* 2013). Hence, there are six dry fracture compliances in total for these two sets of fractures. However, for the calculation of the elastic properties of the 2-D samples, we only need to know four fracture compliances: Z_{N1}, Z_{N2}, Z_{T1}, and Z_{T2} (Guo *et al.* 2017).

The dry fracture compliances Z_{N1}, Z_{N2}, Z_{T1}, and Z_{T2} can be calculated by using the theoretical formulas for 2-D fracture compliances or the general Eshelby's model (Mura 1987; Sevostianov & Kachanov 1999; Kachanov & Sevostianov 2005; Guo *et al.* 2018a). However, the values obtained from these theoretical models have notable discrepancies with respect to the ones inverted from the stiffness coefficients of the dry samples computed from the numerical simulations (Guo *et al.* 2017). One possible reason for the observed discrepancies is the effect of fracture interactions, which are not considered in the theoretical models. To quantify the effects of fracture interactions on the theoretical models, we employ the schemes of the differential effective medium and self-consistent approximation. However, contrary to our expectation, there is nearly no improvement in the agreement between the theoretically predicted and numerically inverted dry fracture compliances. This is consistent with the work of Grechka & Kachanov (2006), who found that in rocks with random distributions of fractures, the influence of fracture interactions is rather small due to the cancellation of the competing effects of stress shielding and amplification, which is also confirmed by Guo *et al.* (2018a). Hence, there should be another reason for the discrepancies. Since the 2-D fractures

Table 1. Dry stiffness coefficients for the samples shown in Fig. 1 provided by the numerical simulations.

	Sample shown in Fig. 1(a)	Sample shown in Fig. 1(b)	Sample shown in Fig. 1(c)	Sample shown in Fig. 1(d)
c_{11} (GPa)	27.18	25.82	40.22	33.77
c_{12} (GPa)	0.27	2.07	0.81	2.38
c_{16} (GPa)	− 0.14	− 0.39	0.28	0.84
c_{22} (GPa)	33.01	32.57	33.86	34.06
c_{26} (GPa)	− 0.49	1.06	0.11	0.87
c_{66} (GPa)	9.56	7.65	12.11	10.27

considered in the theoretical models have elliptical shapes whereas those in the numerical simulations are rectangular, the differences in fracture geometry can be responsible for the discrepancies. To confirm this, we use elliptical fractures in the numerical simulations and compare the results with the theoretical predictions. We observe that the agreement between the theoretically predicted and numerically inverted dry fracture compliances improves greatly (Guo *et al*. 2018a). This verifies that the difference in the fracture geometry considered in the theoretical models and numerical simulations is the primary reason for the discrepancies. However, as this paper is an extension of that published by Guo *et al*. (2017), we keep on using rectangular fractures as Guo *et al*. (2017) for consistency. To compare the theoretical predictions with the numerical simulations, we then compute the dry fracture compliances from the stiffness coefficients of the dry samples obtained from the numerical simulations (shown in Table 1) as follows (Guo *et al*. 2017):

$$Z_{Ni} = S_{ii} - 1/E_b^{2D}, i = 1, 2, \tag{34}$$

$$Z_{T1} + Z_{T2} = S_{66} - 2\left(1 + \nu_b^{2D}\right)/E_b^{2D}, \tag{35}$$

where **S** is the dry compliance matrix of the 2-D samples, which can be inverted from the dry stiffness matrix provided by the numerical simulations; and E_b^{2D} and ν_b^{2D} are the Young's modulus and Poisson ratio of the 2-D background medium, respectively, which have the following relations with the 3-D parameters under the plane strain condition:

$$E_b^{2D} = \frac{E_b}{1 - \nu_b^2}, \tag{36}$$

$$\nu_b^{2D} = \frac{\nu_b}{1 - \nu_b}. \tag{37}$$

It should be noted that eq. (35) only provides the sum of Z_{T1} and Z_{T2}. However, their individual values can be estimated based on the fact that the ratios of the normal to tangential compliance Z_N/Z_T for the considered sets of orthogonal fractures are expected to have close values since they are generated in the same fashion. Hence, Z_{T1} and Z_{T2} can be obtained as follows:

$$Z_{Ti} = Z_{Ni}\frac{Z_{T1} + Z_{T2}}{Z_{N1} + Z_{N2}}, i = 1, 2. \tag{38}$$

The use of the numerically inverted dry fracture compliances in the theoretical model guarantees that the normal and tangential compliances of the dry fractures considered in the numerical simulations and in the theoretical approach are equal, thus allowing the comparisons between the two methodologies. With the dry fracture compliances, the stiffness coefficients of the samples in the low- and high-frequency limits for each manifestation of WIFF can be computed following the steps described above. To obtain the frequency-dependent behaviour of the stiffness coefficients, the values of T and G also need to be calculated, which requires the elastic properties of the fracture infill material. To compare the 3-D theoretical predictions with the 2-D numerical simulations, we calculate the effective elastic properties of the equivalent planar fracture infill material from the properties of the dry 2-D fractures. For each set of the fractures, these properties are calculated through eqs (14) and (15) using the fraction of the fracture set in the rock f_{ci} and the numerically inverted compliances for the dry 2-D fractures Z_{Ni} and Z_{Ti}. Then, these effective fracture infill material properties are used in the calculation of the values of T and G for the planar fracture model, and the value of G for the penny-shaped crack model.

Furthermore, we also need to use the specific surface area and the fracture density of the 2-D fractures in the calculations of T and G, which have the following forms for 2-D rectangular fractures (Kachanov & Sevostianov 2005; Guo *et al*. 2018a):

$$S_i^{2D} = \frac{f_{ci}}{h_{ci}}, i = 1, 2 \tag{39}$$

$$\varepsilon_i = \frac{n_i a^2}{A}, i = 1, 2 \tag{40}$$

where S_1^{2D}, f_{c1}, h_{c1}, ε_1, n_1 are the specific fracture surface area, fraction of fractures in the rock, fracture thickness, fracture density, and number of fractures for the fracture set perpendicular to x-axis. In addition, the subscript 2 represents the corresponding values for the other fracture set, whereas a and A are the fracture radius and area of the sample, respectively.

Using these effective properties of the dry fractures and the other known parameters, the theoretical predictions can be obtained for the three types of fracture geometries (periodic planar fractures, randomly spaced planar fractures and penny-shaped cracks). Since the samples satisfy the plane strain condition, the results of the 3-D theoretical predictions for the stiffness coefficients can then be compared directly with the 2-D numerical simulations.

3.2 Comparison and analysis

It can be found from the numerical simulation results for the considered samples that only four stiffness coefficients (c_{11}, c_{12}, c_{22} and c_{66}) need to be considered for the saturated samples, as the other two stiffness coefficients (c_{16} and c_{26}) turn out to be rather negligible (not shown here for brevity). Hence, in this work we only compare these four stiffness coefficients obtained from the numerical simulations and the theoretical predictions. In addition, the numerical simulations also allow us to verify that all the stiffness coefficients have similar frequency-dependent behaviours for both samples with relatively low symmetry (Figs 1a and b) and high symmetry (Figs 1c and d). This validates our assumption that the frequency-dependent behaviours of all the stiffness coefficients should be similar, even for samples with relatively low symmetry. Hence, in the rest of the work we mostly focus the analysis on the stiffness coefficient c_{22}.

3.2.1 Dispersion and attenuation due to FB-WIFF

Fig. 2 shows the dispersion (variation of the real part with frequency) and attenuation (ratio of the imaginary part to the real part) of c_{22} due to FB-WIFF for the samples shown in Figs 1(a) and (b). As explained before, the non-intersecting periodic planar fracture case is not realizable, hence, we only consider the randomly spaced planar fracture and penny-shaped crack cases for the rock with non-intersecting fractures. It can be seen that, for such rock (Fig. 1a), the theoretical

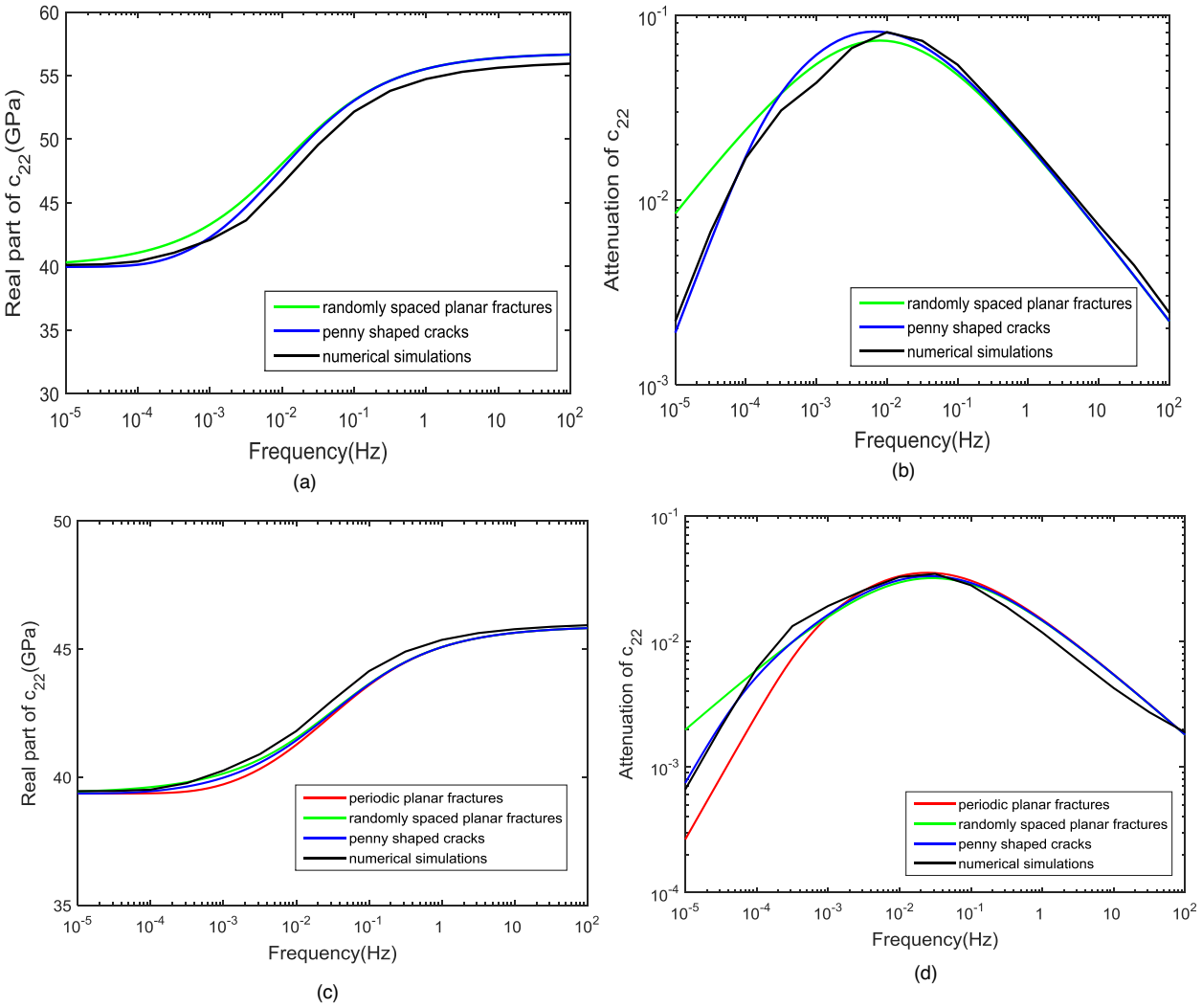

Figure 2. Dispersion and attenuation of c_{22} due to FB-WIFF for the samples containing 20 horizontal and 20 vertical fractures. Panels (a) and (b) show the results for the sample with non-intersecting fractures (Fig. 1a), while panels (c) and (d) correspond to the sample with intersecting fractures (Fig. 1b).

predictions provided by the penny-shaped crack model are in better agreement with the numerical simulations than the randomly spaced planar fracture model (Figs 2a and b). This result is consistent with that obtained for samples with aligned fractures (Guo *et al*. 2018a), which is reasonable as when a seismic wave propagates along the *y*-axis, WIFF primarily occurs between the horizontal fractures and the background for both the non-intersecting and aligned fracture cases. It should also be noted that, even though the fractures in the sample have rectangular geometry (not penny-shaped) and they may interact with each other, good agreement can be found between the results given by the penny-shaped non-interaction crack model and the numerical simulations. This is due to the fact that the effects of the geometry of the fractures and the fracture interactions are taken into account in the theoretical approach, at least partially, by using the numerically-inverted dry fracture compliances.

For the sample with intersecting fractures (Fig. 1b), it can be seen that, also in this case, the theoretical predictions are in good agreement with the numerical simulations (Figs 2c and d). Moreover, the results provided by the penny-shaped crack model match the numerical simulations best. Due to fluid pressure equilibration occurring between connected horizontal and vertical fractures, we use scaled values of T and G to calculate seismic dispersion and attenuation due to FB-WIFF, as explained before. The results depicted by Figs 2(c) and (d) demonstrate that this approach works well and only small discrepancies are observed between the results of the penny-shaped crack model and the numerical simulations.

It is interesting to notice that, for both samples, the attenuation curves at high frequencies given by the theoretical models are similar. This is because the energy dissipation at high frequencies only occurs in the immediate vicinity of the fractures, which implies that, regardless of the geometry of the fractures, the resulting attenuation is controlled by their specific surface area (Gurevich *et al*. 2009; Guo *et al*. 2018a). As we use the same specific surface area obtained from the real geometries of the considered fractures for the theoretical models, their predictions of attenuation at high frequencies coincide.

The samples studied above have an equal number of horizontal and vertical fractures, which can be regarded as a special case characterized by a high degree of symmetry. In order to check if our theoretical models are valid in more general situations, we investigate two more samples with non-intersecting and intersecting fractures (Figs 1c and d). Similar to the samples depicted by Figs 1(a) and (b), these new samples have 20 horizontal fractures; however, in order to reduce their degree of symmetry, they only

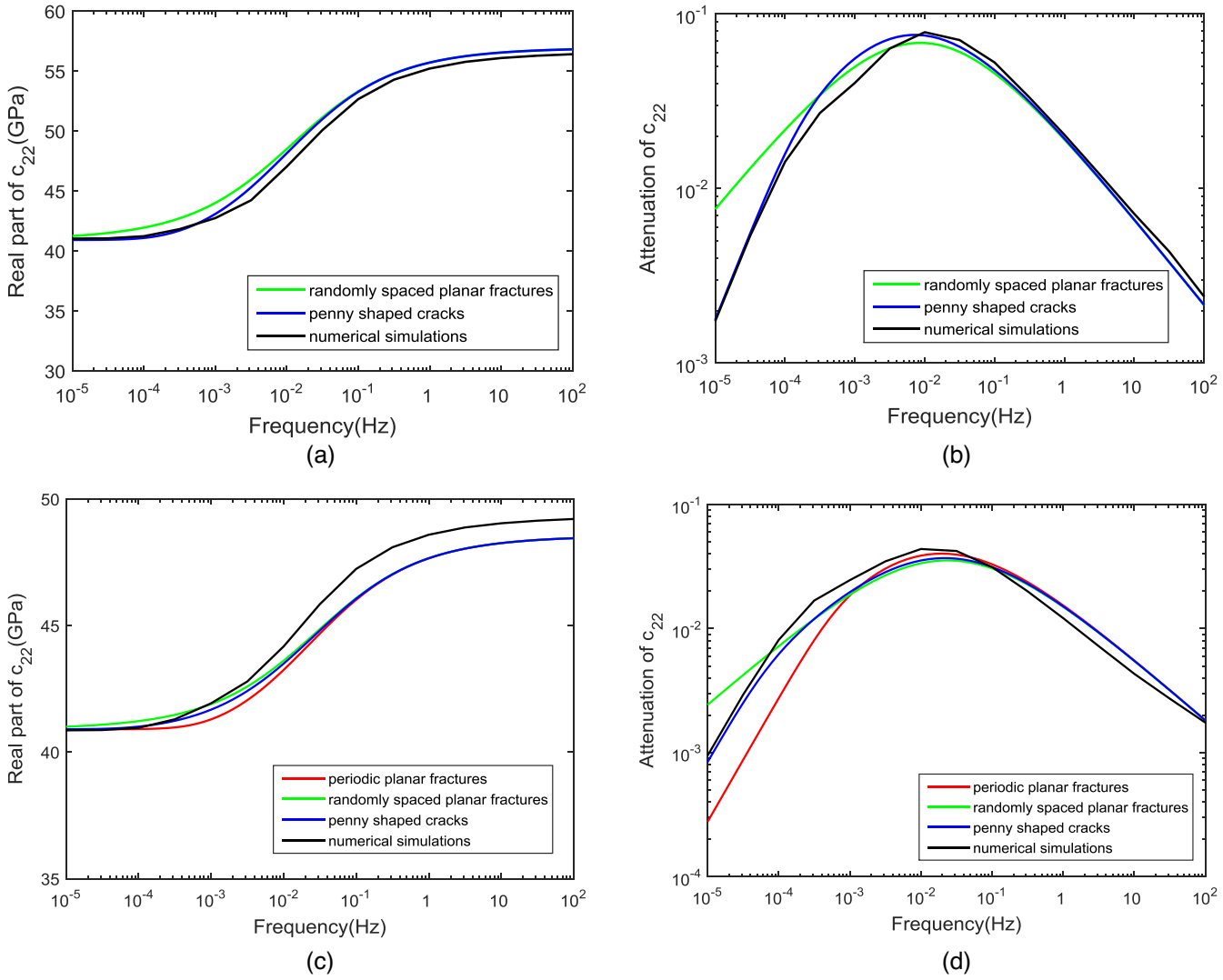

Figure 3. Dispersion and attenuation of c_{22} due to FB-WIFF for the samples containing 10 vertical and 20 horizontal fractures. Panels (a) and (b) show the results for the sample with non-intersecting fractures (Fig. 1c), while panels (c) and (d) correspond to the sample with intersecting fractures (Fig. 1d).

have 10 vertical fractures. Fig. 3 shows the theoretical results for c_{22} along with the numerical simulations. We can see that, again as before, the theoretical predictions given by the penny-shaped crack model match the numerical simulation results best. For the sample with non-intersecting fractures (Fig. 1c), the results are very similar to those corresponding to the sample with 20 vertical fractures (compare Figs 2a and b with Figs 3a and b). This further demonstrates that the influence of vertical fractures on the dispersion and attenuation of c_{22} is rather small in absence of fracture intersections. For the sample with intersecting fractures (Fig. 1d), we see that the value of c_{22} in the high-frequency limit of FB-WIFF is higher than that corresponding to the sample containing 20 vertical fractures (compare Fig. 2c with Fig. 3c). This is produced by an increase in the number of non-intersecting horizontal fractures, which do not release their fluid pressure into connected vertical fractures, thus behaving stiffer.

It can be noted that, in contrast to the case of the sample shown in Fig. 1(b), the theoretically predicted value of c_{22} in the high-frequency limit of FB-WIFF for the sample shown in Fig. 1(d) is slightly lower than the numerical simulation result (Fig. 3c). This is due to the fact that, for the sample shown in Fig. 1(b), nearly every fracture is intersected by at least one orthogonal fracture, and hence the fluid pressure is uniform throughout the whole fracture system. Therefore, the theoretical prediction obtained by saturating the fractures through the use of the anisotropic Gassmann's equation is in good agreement with the numerical simulation results. However, for the sample shown in Fig. 1(d), there are several horizontal fractures that are not intersected by any of the vertical fractures. Hence, the fluid pressure increase in these horizontal fractures cannot be released by flowing into the vertical ones, which results in the effective stiffening of the sample. Thus, the theoretical prediction in the high-frequency limit of this WIFF manifestation based on the anisotropic Gassmann's equation underestimates the numerical simulation results.

As extensively discussed by Guo *et al*. (2017), the characteristic frequency of FB-WIFF is controlled by the diffusivity of the background medium and the fracture radius for both the non-intersecting and intersecting fracture cases. When the diffusion length computed using the physical properties of the background is comparable to the fracture radius, maximum seismic attenuation due to fluid flow between the fractures and the background occurs. It is interesting to note here that, as can be seen in Figs 2 and 3, there is a slight

shift of the characteristic frequency of FB-WIFF between the non-intersecting and intersecting fracture cases. For the non-intersecting fracture case, when a seismic wave propagates in the direction perpendicular to one set of the fractures, fluid flow primarily occurs between this set of fractures and the background medium. However, in the intersecting fracture case, as the fluid pressure is equilibrated between connected horizontal and vertical fractures, the fluid flow between connected fractures that are parallel to the propagation direction and the background medium will also be significant (Rubino *et al*. 2014). Hence, the different fluid flow characteristics between the non-intersecting and intersecting fracture cases is expected to be responsible for the slight shift of the characteristic frequency of FB-WIFF between these two cases.

3.2.2 Dispersion and attenuation due to FF-WIFF

Fig. 4 shows the dispersion and attenuation of c_{22} due to FF-WIFF for the samples depicted by Figs 1(b) and (d). We see that, in contrast to the case of FB-WIFF, the theoretical predictions given by the periodic planar fracture model match the numerical simulations best. As explained before, the theoretical predictions for FF-WIFF are based on an effective background medium approach. For c_{22}, the effective background medium is composed of the saturated background as the solid phase and the fractures along the y-axis as the pore space. The good agreement between the theoretical predictions provided by the periodic planar fracture model and the numerical simulations indicates that the behaviour of the fractures is largely consistent with that of periodic planar fractures in an effective background medium when FF-WIFF occurs. Further inspection of the curves shown in Fig. 4 indicates that the discrepancies between the theoretical predictions of the planar fracture model and the numerical simulations are primarily found at low frequencies. This is probably due to the fact that FB-WIFF does not vanish completely at the low frequencies of FF-WIFF. Hence, these two manifestations of WIFF interact with each other for such frequencies, an effect that is not considered in the theoretical predictions presented in this work. Moreover, it is worthwhile to mention here that the characteristic frequency of FF-WIFF is controlled by the diffusivity of the effective background medium and the fracture radius, as discussed in Guo *et al*. (2017). The FF-WIFF will induce maximum seismic attenuation when the diffusion length is comparable to the fracture radius.

It is important to remark that the effective background medium used here is anisotropic, whereas the background medium for FB-WIFF is isotropic. As discussed above, the theoretical models were originally developed for fractures embedded in an isotropic background medium. Hence, to take into account the anisotropic properties of the effective background medium and, at the same time, to keep our approach simple to apply, we use the properties of the anisotropic effective background medium in the considered direction of wave propagation to replace the original isotropic background properties. This ignores the influence of the properties of the anisotropic background medium in other directions on the FF-WIFF. This, in turn, may be another source of discrepancies between the theoretical predictions and the numerical simulations. Furthermore, the porosity in the effective background medium is of the same order of magnitude as the fracture porosity. However, our theoretical models assume that the fracture porosity should be much smaller than the porosity in the effective background medium. Hence, this assumption is violated here. This can also cause some errors in the theoretical predictions. In addition, the fractures are assumed to be interconnected to each other in the theoretical model, whereas some fractures are not connected to other fractures in the investigated samples, especially for that shown in Fig. 1(d). This influences the fluid flow characteristics between fractures and hence can be another reason for the discrepancies observed between the theoretical predictions and numerical simulations. All these important points will require detailed analysis in the future.

3.2.3 Dispersion and attenuation of all the stiffness coefficients for the full frequency range

In Fig. 5, we compare the theoretical predictions and numerical simulations of the dispersion and attenuation of all the stiffness coefficients for the full frequency range for samples with non-intersecting (Fig. 1a) and intersecting fractures (Fig. 1b). The theoretical predictions for the effects caused by FB-WIFF are given by the penny-shaped crack model, whereas the periodic planar fracture model is used for representing those caused by FF-WIFF. For brevity, the results for the samples shown in Figs 1(c) and (d) are not included, as they are qualitatively similar to those corresponding to the chosen samples.

For the sample with non-intersecting fractures, we can see good agreement between the theoretical predictions and the numerical simulations (Figs 5a and b). We observe that, in contrast to c_{11} and c_{22}, the real part of c_{12} decreases with frequency, which corresponds to negative attenuation. However, c_{12} does not control any type of seismic wave by itself and, hence, the attenuation of seismic waves propagating through the probed medium remains positive even though that of c_{12} is negative. Furthermore, we can notice in the numerical simulations a small shift of the characteristic frequency of c_{12} compared to that of c_{11} and c_{22}. In the theoretical predictions, we assume that all the stiffness coefficients have nearly the same characteristic frequency. This inconsistency is probably due to fracture interactions, which are not taken into account by the theoretical predictions. In addition, small discrepancies can be found between the theoretical predictions and the numerical simulations for c_{11} at low frequencies. This is likely to be due to fluid diffusion interaction effects at low frequencies. As the vertical fractures tend to concentrate in small areas (Fig. 1a), fluid diffusion interaction can easily occur between adjacent vertical fractures at low frequencies (Müller & Rothert 2006). From the point of view of the diffusion process, adjacent vertical fractures tend to merge, which results in an apparent increase of the effective length of fractures at low frequencies. This is not considered in the theoretical predictions, which may cause the small discrepancies observed for c_{11} at low frequencies. To verify this, we increase the radii of the vertical fractures by a factor of 1.5 when calculating the value of T needed for the theoretical approach. The resulting estimates, which are shown as circles in Figs 5(a) and (b), improve the agreement with the numerical simulations for c_{11}.

It is interesting to note that the shear modulus c_{66} shows small dispersion and attenuation in the numerical simulations for the sample with non-intersecting fractures. In the theoretical predictions, it was assumed that *SV*-waves propagating along the x- or y- axis do not perturb the fluid pressure field. This, in turn, implies that the shear modulus c_{66} for the saturated sample is equal to that for the dry sample and is independent of frequency. However, in the numerical simulations, due to the heterogeneities of the fractured sample, a smooth fluid pressure gradient is induced and, hence, fluid flow occurs causing slight dispersion and attenuation of c_{66}. This phenomenon was also observed by Caspari *et al*. (2016).

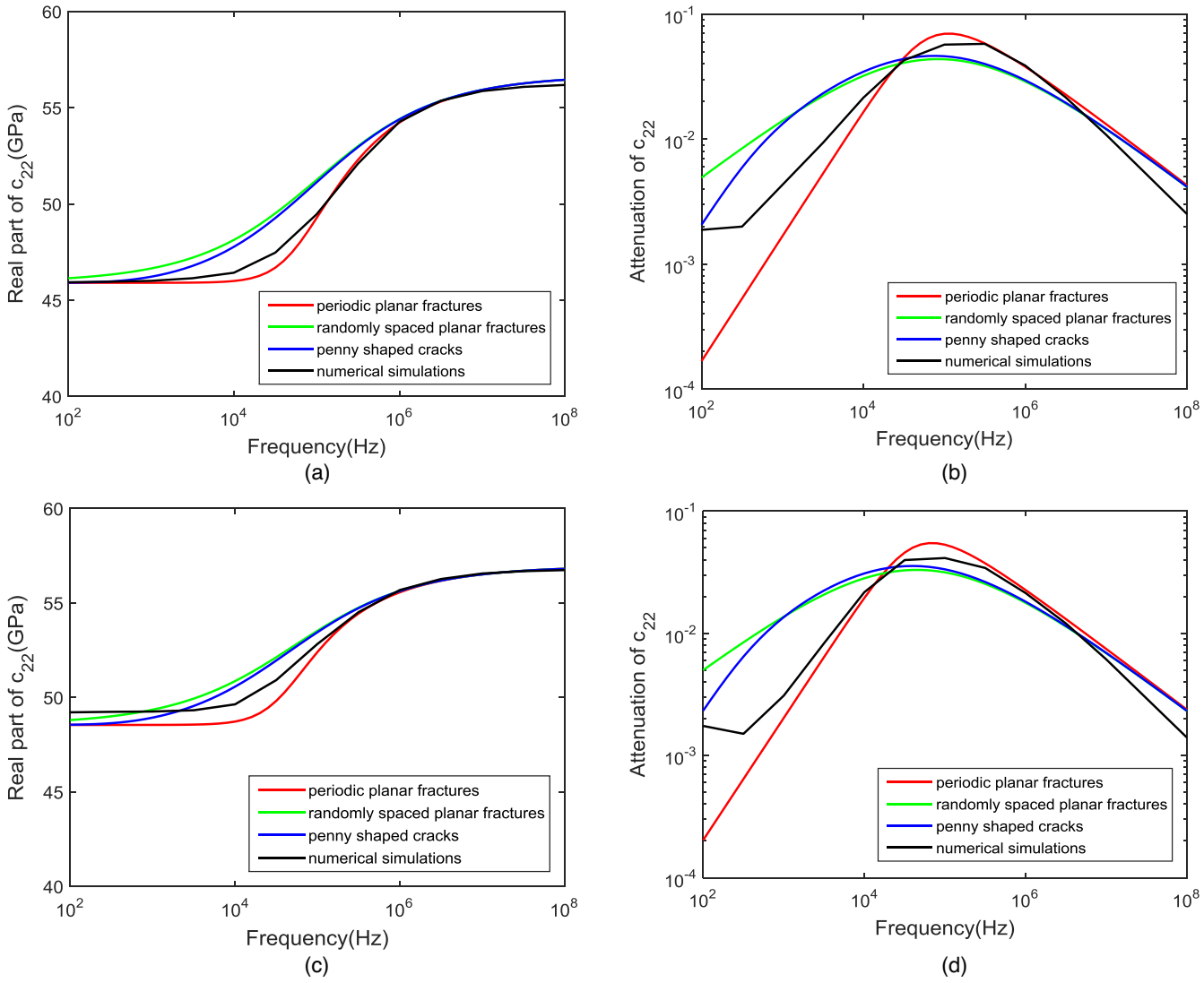

Figure 4. Dispersion and attenuation of c_{22} due to FF-WIFF. Panels (a) and (b) depict the results for the sample shown in Fig. 1(b), while panels (c) and (d) correspond to the sample shown in Fig. 1(d).

For the sample with intersecting fractures, good agreement is also observed between the theoretical predictions and the numerical simulations. We see small discrepancies for c_{12}, especially for the dispersion and attenuation due to FF-WIFF. This is primarily due to the fact that the theoretically-predicted value of c_{12} in the high-frequency limit for this WIFF manifestation is slightly lower than the value given by the numerical simulations. Hence, the corresponding theoretically-predicted dispersion and attenuation are slightly larger than the numerical simulation results. In addition, it is interesting to notice that for this sample the dispersion and attenuation of c_{66} in the numerical simulations turned out to be higher than for the sample with non-intersecting fractures. This means that the fluid pressure gradient induced by *SV*-waves propagating along the *x*- or *y*- axis for samples with intersecting fractures is much larger than for samples with non-intersecting fractures.

3.2.4 Anisotropic properties

Following Guo *et al*. (2017), it is interesting to compare Thomsen's style anisotropy parameters given by the theoretical predictions and the numerical simulations. Using the stiffness coefficients provided by the theoretical predictions and the numerical simulations, the anisotropy parameters $\varepsilon^{(3)}$ and $\delta^{(3)}$ are then calculated using eqs (29) and (30) for the samples shown in Figs 1(a) and (b). For the sample with non-intersecting fractures, Fig. 6(a) shows that the theoretical predictions are in overall good agreement with the numerical simulations. Some small discrepancies can be seen, which are primarily caused by the inaccurate value of c_{11} given by the theoretical predictions. If we use the improved value of c_{11} (circles in Fig. 5a) to calculate the anisotropy parameters (circles in Fig. 6a), the discrepancies between the theoretical predictions and the numerical simulations get smaller, especially for $\varepsilon^{(3)}$. For the sample with intersecting fractures, we also see overall good agreement between the theoretical predictions of the anisotropy parameters and the numerical simulations (Fig. 6b). In particular, we see that the theoretical prediction of $\varepsilon^{(3)}$ matches very well with the numerical simulations. On the other hand, while the theoretical prediction of $\delta^{(3)}$ is systematically slightly lower than the numerical simulations, their variations with frequency are similar. The observed differences are mainly due to the discrepancies in the coefficients c_{12} and c_{66}.

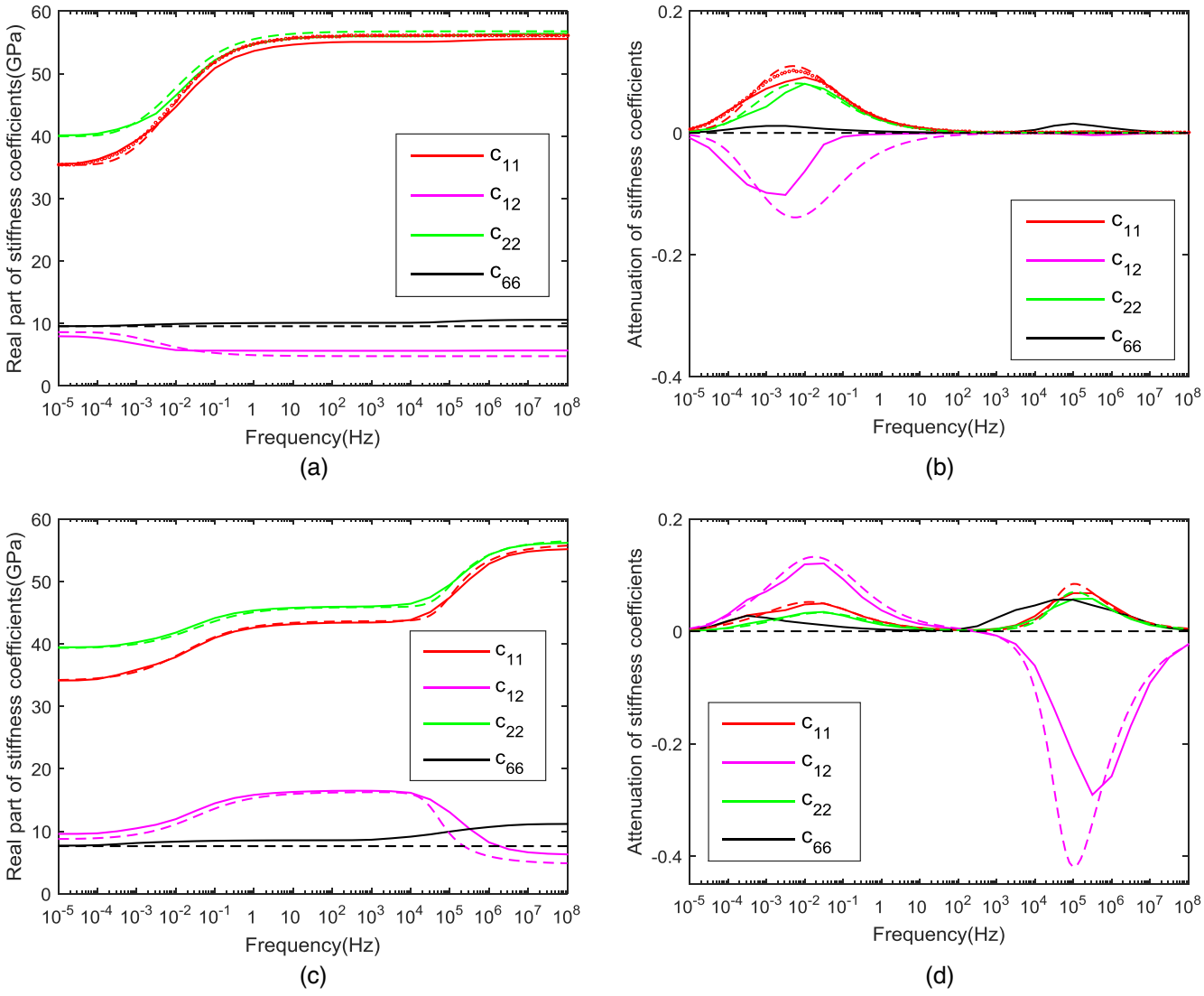

Figure 5. Theoretical predictions (dashed lines) and numerical simulations (solid lines) for all the stiffness coefficients and for the full frequency range. Panels (a) and (b) depict the results for the sample shown in Fig. 1(a), while panels (c) and (d) correspond to the sample shown in Fig. 1(b). The circles in panels (a) and (b) represent the results for c_{11} considering increased radii of the vertical fractures to account for fluid pressure diffusion interactions.

To further compare the anisotropic properties given by the theoretical predictions and the numerical simulations, we calculate the phase velocity and attenuation of *qP*- and *qSV*-waves as functions of incidence angle. For the sample with non-intersecting fractures (Fig. 1a), we know from Fig. 5 that the largest discrepancies between the theoretical predictions and the numerical simulations occur for frequencies close to the characteristic frequency of FB-WIFF (∼0.01 Hz). Hence, we compare the predictions at this particular frequency. We observe in Figs 7(a) and (b) that the angle-dependent velocities provided by the theoretical prediction and the numerical simulations are in very good agreement, whereas some discrepancies arise in the case of attenuation. This is primarily due to the differences in c_{12} and c_{66} given by the two approaches. In the case of the sample with intersecting fractures (Fig. 1b), we compare the angle-dependent predictions at a frequency of 10^5 Hz, for which the largest discrepancies took place (Fig. 5). Figs 7(c) and (d) indicate that relatively good agreement between the theoretical predictions and the numerical simulations also occurs in this case. However, significant discrepancies between the two approaches arise, especially for the *qSV*-wave at incidence angles of 0° and 90°. The observed discrepancies are also primarily due to the differences in c_{12} and c_{66}. In particular, the shear modulus c_{66} is frequency-independent in the theoretical predictions, whereas it shows some frequency-dependency in the numerical simulations due to the heterogeneity of the sample (Caspari *et al*. 2016). Indeed, if we assume no frequency-dependency for c_{66} in the numerical simulations, the agreement between theoretical predictions and numerical simulations improves greatly (not shown here for brevity). Hence, in the future, the theoretical model can be further developed to incorporate the frequency-dependency of the shear modulus c_{66}. This should greatly reduce the discrepancies between theoretical predictions and numerical simulations.

It is interesting to note here that the attenuation of *P*-waves propagating with an incidence angle of 45° vanishes in the theoretical predictions for the sample with intersecting fractures. This is due to the fact that, when the *P*-wave propagates in this direction, it will generate the same fluid pressure in the horizontal and vertical fractures and, hence, fluid flow within connected fractures is

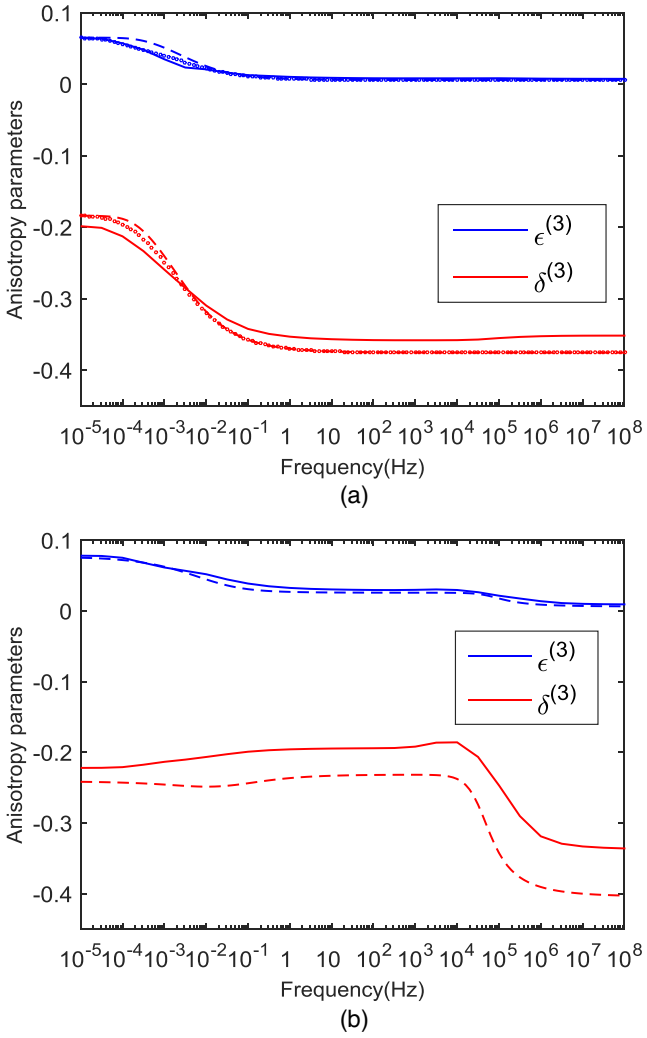

Figure 6. Anisotropic parameters calculated using the stiffness coefficients provided by the theoretical predictions (dashed lines) and the numerical simulations (solid lines). Panels (a) and (b) depict the results for the samples shown in Figs 1(a) and (b), respectively. The theoretical predictions considering increased radii of the vertical fractures to account for fluid diffusion interactions are also given in panel (a) as circles.

negligible. However, this attenuation value does not completely vanish in the case of the numerical simulations, which is also due to the frequency dependence of c_{66}.

Hence, we have compared the angle dependence of the phase velocity and attenuation of *qP*- and *qSV*-waves for the two samples (Figs 1a and b) at the frequencies that showed the largest discrepancies between the theoretical predictions and numerical simulations. For other frequencies, the discrepancies are expected to be much smaller. These results, combined with the comparison of the anisotropic parameters, allow us to conclude that the anisotropic properties given by the theoretical predictions and numerical simulations are in overall good agreement with each other.

4 DISCUSSION

In this paper, we considered seismic dispersion and attenuation in saturated porous rocks containing two orthogonal sets of non-intersecting and intersecting mesoscopic fractures. To validate our theoretical model, we compared its predictions with corresponding numerical simulations. However, due to the high computational cost of 3-D numerical simulations, we only considered 2-D cases and compare the results with 3-D theoretical predictions. To enable this comparison, we obtained effective parameters for the 2-D samples and then substituted them into the 3-D theoretical model, as shown in Section 3.1. The good agreement between the theoretical predictions and the numerical simulations means that a model designed for axisymmetric penny-shaped cracks is also valid for slit 2-D fractures (especially for the FB-WIFF effects) (Fig. 8). This observation is a surprise to the authors, and suggests that the characteristics of seismic dispersion and attenuation are not particularly sensitive to the in-plane shape of the fractures. Recall that in the theoretical model, the crack diameter controls the characteristic frequency of the dispersion and attenuation (e.g. Guo *et al*. 2017). For the slit fractures modelled in numerical simulations (Fig. 8), the corresponding length scale parameter is slit length L, while fracture 'depth' D is infinite. Thus, the agreement between theory and simulations also means that the characteristics of the dispersion and attenuation are controlled by the smaller of the two fracture length parameters L, and are relatively insensitive to the larger of these parameters D. A similar observation was made by Barbosa *et al*. (2017) through comparisons of 2-D and 3-D numerical simulations for very simple fracture networks.

Up until now, a number of theoretical models have been proposed to study seismic wave propagation in saturated porous rocks with multiple sets of fractures (e.g. Liu *et al*. 2006; Chapman 2009). However, these models assume that the fractures are hydraulically connected to the background medium, but unconnected to each other. Hence, effects due to fluid flow between the background medium and the fractures (FB-WIFF) are considered, whereas those related to flow within connected fractures (FF-WIFF) are neglected (e.g. Liu *et al*. 2006; Chapman 2009). Thus, these models should predict frequency-dependent elastic properties for the non-intersecting fracture cases similar to those provided by our theoretical model. However, in presence of connected fractures these models cannot account for the corresponding effects on both FB- and FF-WIFF. A detailed comparison between these models and the one proposed in this paper will be carried out in the future.

It is important to remark here that, in presence of intersecting fractures, the degree of seismic dispersion and attenuation caused by FB-WIFF is significantly reduced due to the fluid pressure communication within connected fractures, as shown in Fig. 5. In addition, the velocity anisotropy of such rocks can also be significantly reduced due to variations of the stiffening effects of the fracture fluid in response to FF-WIFF (Rubino *et al*. 2017). Hence, it is of great importance to consider both manifestations of WIFF when interpreting seismic data from fractured reservoirs. This, in turn, may provide the possibility to extract information on the connectivity degree of fracture networks from seismic recordings.

5 CONCLUSIONS

In this work, we proposed a theoretical approach to describe seismic dispersion and attenuation of saturated porous rocks containing two orthogonal sets of non-intersecting or intersecting fractures. The methodology was based on theoretical models for rocks with aligned fractures, and three types of fracture geometries were considered, namely, periodic planar fractures, randomly spaced planar fractures and penny-shaped cracks. For rocks with non-intersecting fractures, seismic dispersion and attenuation are produced by FB-WIFF, a process similar to that arising in rocks containing

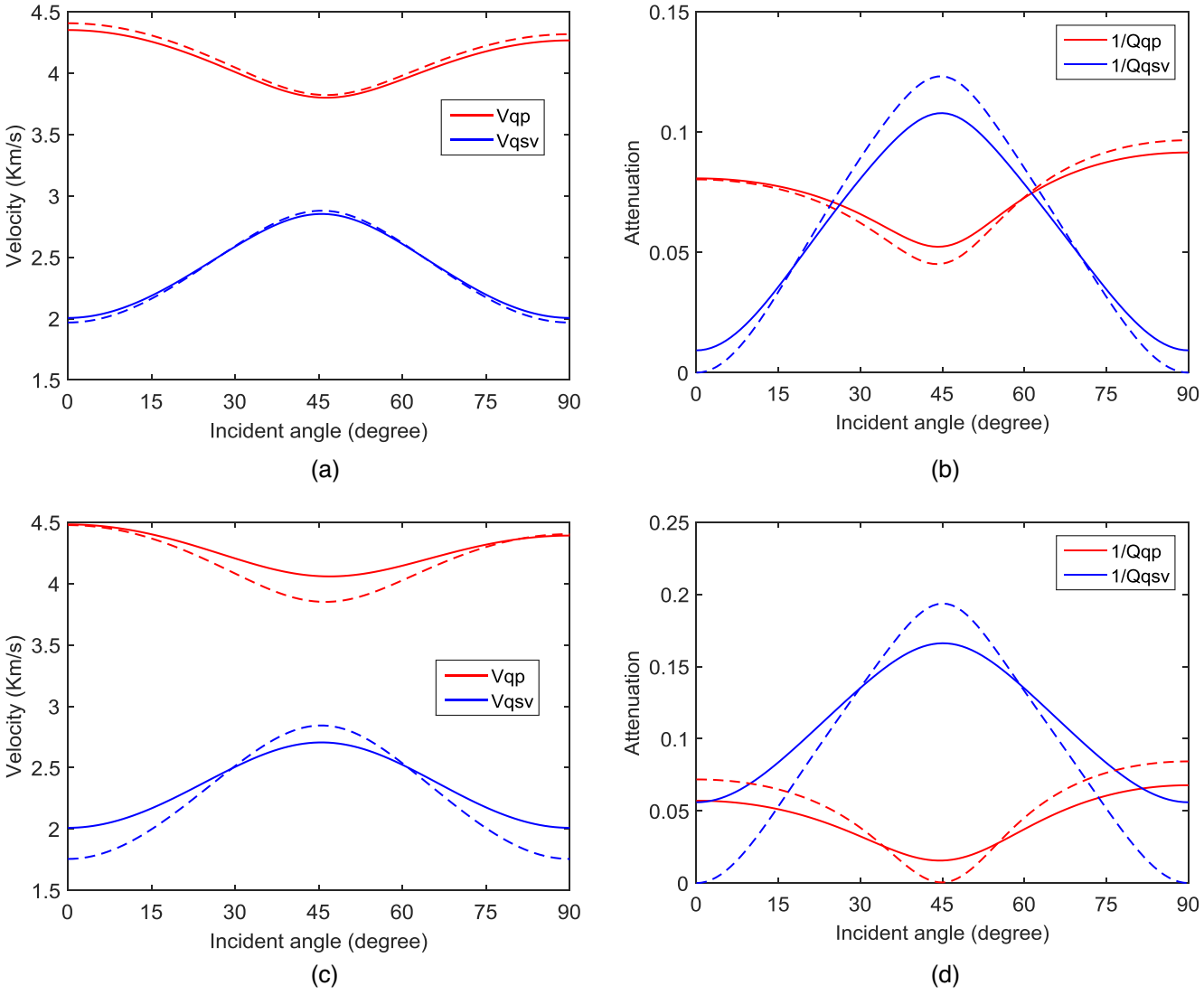

Figure 7. Phase velocity and attenuation of *qP*- and *qSV*-waves as functions of incidence angle given by the theoretical predictions (dashed lines) and the numerical simulations (solid lines). Panels (a) and (b) show the results for the sample with non-intersecting fractures (Fig. 1a) at a frequency of 0.01 Hz, whereas panels (c) and (d) correspond to the sample with intersecting fractures (Fig. 1b) and a frequency of 10^5 Hz.

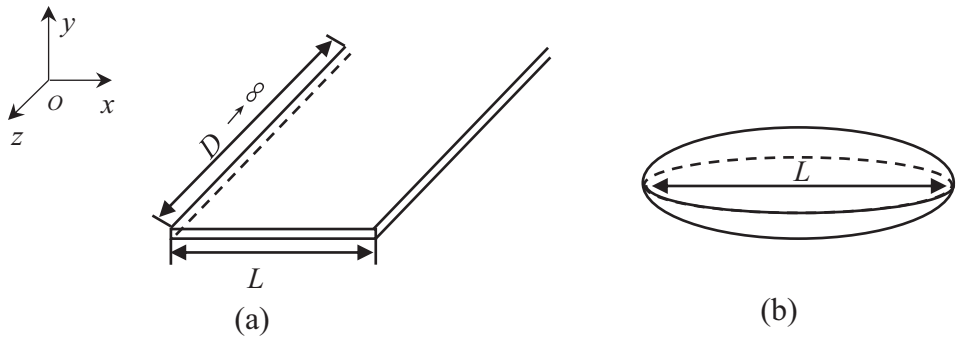

Figure 8. Schematic representation of the 2-D slit fractures considered in the numerical simulations (a), and the penny-shaped cracks (oblate spheroid) considered in the theoretical predictions (b).

aligned fractures. Hence, the theoretical models for aligned fractures can be directly extended to this case for computing the *P*-wave moduli in the directions perpendicular to the two fracture sets, from where the remaining elastic moduli are derived. For rocks with intersecting fractures, FF-WIFF also occurs at higher frequencies. Similar to the non-intersecting fracture case, the effects due to FB-WIFF can be computed by extending the theoretical models for aligned fractures. Conversely, for computing the effects caused by FF-WIFF, an effective background medium was introduced. The theoretical models for aligned fractures were then used, with the

original background replaced by the effective medium, where the fractures perpendicular to the propagation direction were immersed.

2-D synthetic rock samples containing two orthogonal sets of fractures with varying degrees of intersections were then explored. To do this, apart from the theoretical predictions, numerical simulations were also carried out, which consist of an upscaling method in the framework of Biot's quasi-static equations of poroelasticity. The results show that the theoretical predictions are in overall good agreement with the numerical simulations. For the effects caused by FB-WIFF, the theoretical model for penny-shaped cracks matches the numerical simulations best, whereas for those produced by FF-WIFF the model for periodic planar fractures is the most suitable one. Furthermore, we also observe good agreement between the theoretical predictions and the numerical simulations of the anisotropic properties. The proposed theoretical approach is convenient to apply in practice, and is applicable not only to 2-D but also to 3-D fracture systems. Therefore, it has the potential to constitute a powerful tool to assist in the seismic characterization of fracture systems.

ACKNOWLEDGEMENTS

The authors are grateful to the sponsors of the Curtin Reservoir Geophysics Consortium (CRGC) for the financial support.

REFERENCES

Bakulin, A., Grechka, V. & Tsvankin, I., 2000a, Estimation of fracture parameters from reflection seismic data - Part I: HTI model due to a single fracture set, *Geophysics,* **65**(6), 1788–1802.

Bakulin, A., Grechka, V. & Tsvankin, I., 2000b, Estimation of fracture parameters from reflection seismic data - Part II: Fractured models with orthorhombic symmetry, *Geophysics,* **65**(6), 1803–1817.

Bakulin, A., Grechka, V. & Tsvankin, I., 2000c, Estimation of fracture parameters from reflection seismic data - Part III: Fractured models with monoclinic symmetry, *Geophysics,* **65**(6), 1818–1830.

Barbosa, N.D., Rubino, J.G., Caspari, E., Guo, J., Gurevich, B. & Holliger, K., 2017, Hybrid modelling of 3D fractured media based on 2D numerical simulations: aligned fractures case, in *SEG International Exposition and 87th Annual Meeting*, 24 – 29 September, Houston, USA, SEG, pp. 4200–4204.

Basquet, R., Rennan, L., Ringen, J. & Wennberg, O.P., 2008. Fluid flow simulations on core samples containing natural fractures and stylolites, in *EAGE Conference and Exhibition*, 9–12 June, Rome, Italy, European Association of Geoscientists & Engineers, E007.

Biot, M.A., 1941. General theory of three-dimensional consolidation, *J. Appl. Phys.*, **12**(2), 155–164.

Brajanovski, M., Gurevich, B. & Schoenberg, M., 2005. A model for *P*-wave attenuation and dispersion in a porous medium permeated by aligned fractures, *Geophys. J. Int.*, **163**(1), 372–384.

Bristow, J.R., 1960. Microcracks, and the static and dynamic elastic constants of annealed and heavily cold-worked metals, *British Journal of Applied Physics,* **11**(11), 81–85.

Carcione, J.M., Gurevich, B., Santos, J.E. & Picotti, S., 2013. Angular and frequency-dependent wave velocity and attenuation in fractured porous media, *Pure appl. Geophys.*, **170**(11), 1673–1683.

Caspari, E., Milani, M., Rubino, J.G., Müller, T.M., Quintal, B. & Holliger, K., 2016. Numerical upscaling of frequency-dependent P- and S-wave moduli in fractured porous media, *Geophysical Prospecting,* **64,** 1166–1179.

Chapman, M., 2003. Frequency-dependent anisotropy due to meso-scale fractures in the presence of equant porosity, *Geophys. Prospect.*, **51**(5), 369–379.

Chapman, M., 2009, Modeling the effect of multiple sets of mesoscale fractures in porous rock on frequency-dependent anisotropy, *Geophysics*, **74**(6), D97–D103.

Che, X., Qiao, W., Liu, P., Ju, X. & Lu, J., 2015. Identification of fractures in carbonates using sonic imaging logs example from the central of East European plain, *J. acoust. Soc. Am.*, **137**(4), 2403–2404.

Collet, O., Gurevich, B., Madadi, M. & Pervukhina, M., 2014. Modeling elastic anisotropy resulting from the application of triaxial stress, *Geophysics*, **79**(5), C135–C145.

Far, M.E., Thomsen, L. & Sayers, C.M., 2013. Seismic characterization of reservoirs with asymmetric fractures, *Geophysics*, **78**(2), N1–N10.

Gao, D., 2013. Integrating 3D seismic curvature and curvature gradient attributes for fracture characterization: Methodologies and interpretational implications, *Geophysics*, **78**(2), O21–O31.

Gale, J.F.W., Reed, R.M. & Holder, J., 2007. Natural fractures in the Barnett Shale and their importance for hydraulic fracture treatments, *AAPG Bull.*, **91**(4), 603–622.

Galvin, R.J. & Gurevich, B., 2006. Interaction of an elastic wave with a circular crack in a fluid-saturated porous medium, *Appl. Phys. Lett.*, **88**(6), 061918-1–061918-3.

Galvin, R.J. & Gurevich, B., 2007. Scattering of a longitudinal wave by a circular crack in a fluid-saturated porous medium, *Int. J. Solids Struct.*, **44**(22–23), 7389–7398.

Galvin, R.J. & Gurevich, B., 2009. Effective properties of a poroelastic medium containing a distribution of aligned cracks, *J. geophys. Res.*, **114**(B7), B07305-1–B07305-11.

Glubokovskikh, S., Gurevich, B., Lebedev, M., Mikhaltsevitch, V. & Tan, S., 2016. Effect of asperities on stress dependency of elastic properties of cracked rocks, *Int. J. Eng. Sci.*, **98**, 116–125.

Grechka, V. & Kachanov, M., 2006. Effective elasticity of rocks with closely spaced and intersecting cracks, *Geophysics*, **71**(3), D85–D91.

Guo, J., Rubino, J.G., Glubokovskikh, S. & Gurevich, B., 2017. Effects of fracture intersections on seismic dispersion: theoretical predictions versus numerical simulations, *Geophys. Prospect.*, **65**(5), 1264–1276.

Guo, J., Rubino, J.G., Barbosa, N.D., Glubokovskikh, S. & Gurevich, B., 2018a. Seismic dispersion and attenuation in saturated porous rocks with aligned fractures of finite thickness: Theory and numerical simulations—Part 1: *P*-wave perpendicular to the fracture plane, *Geophysics*, **83**(1), WA49–WA62.

Guo, J., Rubino, J.G., Barbosa, N.D., Glubokovskikh, S. & Gurevich, B., 2018b. Seismic dispersion and attenuation in saturated porous rocks with aligned fractures of finite thickness: theory and numerical simulations—Part 2: Frequency-dependent anisotropy, *Geophysics*, **83**(1), WA63–WA71.

Gurevich, B., 2003. Elastic properties of saturated porous rocks with aligned fractures, *J. Appl. Geophys.*, **54**(3–4), 203–218.

Gurevich, B., Brajanovski, M., Galvin, R.J., Müller, T.M. & Toms-Stewart, J., 2009. *P*-wave dispersion and attenuation in fractured and porous reservoirs—poroelasticity approach, *Geophys. Prospect.*, **57**(2), 225–237.

Hudson, J.A., 1981. Wave speeds and attenuation of elastic waves in material containing cracks, *Geophys. J. R. astr. Soc.*, **64**(1), 133–150.

Huo, D. & Gong, B., 2010. Discrete modelling and simulation on potential leakage through fractures in CO_2 sequestration, in *SPE Annual Technical Conference and Exhibition*, 19–22 September, Florence, Italy, Society of Petroleum Engineers, SPE 135507.

Johnson, D.L., 2001. Theory of frequency dependent acoustics in patchy-saturated porous media, *J. acoust. Soc. Am.*, **110**(2), 682–694.

Kachanov, M. & Sevostianov, I., 2005. On quantitative characterization of microstructures and effective properties, *Int. J. Solids Struct.*, **42**(2), 309–336.

Kuster, G.T. & Toksöz, M.N., 1974. Velocity and attenuation of seismic waves in two-phase media: part I. Theoretical formulations, *Geophysics*, **39**(5), 587–606.

Lambert, G., Gurevich, B. & Brajanovski, M., 2006. Attenuation and dispersion of *P*-waves in porous rocks with planar fractures: comparison of theory and numerical simulations, *Geophysics*, **71**(3), N41–N45.

Lisjak, A., Figi, D. & Grasselli, G., 2014. Fracture development around deep underground excavations: insights from FDEM modelling, *J. Rock Mech. Geotech. Eng.*, **6**(6), 493–505.

Liu, C., Mehrabian, A. & Abousleiman, Y., 2017. Poroelastic dual-porosity/dual-permeability after-closure pressure-curves analysis in hydraulic fracturing, *SPE J.*, **22**(1), 198–218.

Liu, E. & Martinez, A., 2012. *Seismic Fracture Characterization*, EAGE Publications bv.

Liu, E., Chapman, M., Zhang, Z & Queen, J.H., 2006. Frequency-dependent anisotropy: effects of multiple fracture sets on shear-wave polarizations, *Wave Motion*, **44**(1), 44–57.

Mavko, G., Mukerji, T. & Godfrey, N., 1995. Predicting stress-induced velocity anisotropy in rocks, *Geophysics*, **60**(4), 1081–1087.

Mavko, G., Mukerji, T. & Dvorkin, J., 2009. *The Rock Physics Handbook*, Cambridge Univ. Press.

Müller, T.M. & Rothert, E., 2006. Seismic attenuation due to wave-induced flow: why Q in random structures scales differently, *Geophys. Res. Lett.*, **33**(16), L16305.

Müller, T.M., Gurevich, B. & Lebedev, M., 2010. Seismic wave attenuation and dispersion resulting from wave-induced flow in porous rocks – A review, *Geophysics*, **75**(5), 75A147–75A164.

Mura, T., 1987. *Micromechanics of Defects in Solids*, Martinus Nijhoff Publishers.

Nakagawa, S. & Schoenberg, M.A., 2007. Poroelastic modeling of seismic boundary conditions across a fracture, *J. Acoust. Soc. Am.*, **122**(2), 831–847.

Neuzil, C.E., 2013. Can shale safely host U.S. nuclear waste?, *EOS, Trans. Am. geophys. Un.*, **94**(30), 261–262.

Ostojic, J., Rezaee, R. & Bahrami, H., 2012. Production performance of hydraulic fractures in tight gas sands, a numerical simulation approach, *J. Pet. Sci. Eng.*, **88–89**, 75–81.

Pride, S.R. & Berryman, J.G., 2003. Linear dynamics of double-porosity dual-permeability materials. II. Fluid transport equations, *Phys. Rev. E*, **68**(3), 03660-1–036604-10.

Rubino, J.G., Guarracino, L., Müller, T.M. & Holliger, K., 2013. Do seismic waves sense fracture connectivity?, *Geophys. Res. Lett.*, **40**(4), 692–696.

Rubino, J.G., Müller, T.M., Guarracino, L., Milani, M. & Holliger, K., 2014. Seismoacoustic signatures of fracture connectivity, *J. geophys. Res.*, **119**(3), 2252–2271.

Rubino, J.G., Caspari, E., Müller, T.M., Milani, M., Barbosa, N. D. & Holliger, K., 2016. Numerical upscaling in 2-D heterogeneous poroelastic rocks: anisotropic attenuation and dispersion of seismic waves, *J. geophys. Res.*, **121**(9), 6698–6721.

Rubino, J.G., Caspari, E., Müller, T.M. & Holliger, K., 2017. Fracture connectivity can reduce the velocity anisotropy of seismic waves, *Geophys. J. Int.*, **210**(1), 223–227.

Sassen, D.S. & Everett, M.E., 2009. 3D polarimetric GPR coherency attributes and full-waveform inversion of transmission data for characterizing fractured rock, *Geophysics*, **74**(3), J23–J34.

Schoenberg, M., 1980. Elastic wave behavior across linear slip interfaces, *J. acoust. Soc. Am.*, **68**(5), 1516–1521.

Schoenberg, M. & Douma, J., 1988. Elastic wave propagation in media with parallel fractures and aligned cracks, *Geophys. Prospect.*, **36**(6), 571–590.

Schoenberg, M. & Sayers, C.M., 1995. Seismic anisotropy of fractured rock, *Geophysics*, **60**(1), 204–211.

Sevostianov, I. & Kachanov, M., 1999. Compliance tensors of ellipsoidal inclusions, *Int. J. Fract.*, **96**(1), 3–7.

Tsvankin, I., 1997. Anisotropic parameters and *P*-wave velocity for orthorhombic media, *Geophysics*, **62**(4), 1292–1309.

Vlastos, S., Liu, E., Main, I.G. & Narteau, C., 2007. Numerical simulation of wave propagation in 2-D fractured media: scattering attenuation at different stages of the growth of a fracture population, *Geophys. J. Int.*, **171,** 865–880.

Walsh, J.B., 1965. The effect of cracks on the compressibility of rock, *J. Geophys. Res.*, **70**(2), 381–389.

Wang, S., Li, X.-Y., Qian, Z., Di, B. & Wei, J., 2007. Physical modelling studies of 3-D *P*-wave seismic for fracture detection, *Geophys. J. Int.*, **168**(2), 745–756.

Yuan, S., Deangelo, M.V. & Hardage, B.A., 2014. Interpretation of fractures and joint inversion using multicomponent seismic data—Marcellus Shale example, *Interpretation*, **2**(2), SE55–SE62.

Zazoun, R.S., 2013. Fracture density estimation from core and conventional well logs data using artificial neural networks: The Cambro-Ordovician reservoir of Mesdar oil field, Algeria, *J. Afr. Earth Sci.*, **83**, 55–73.

Zeeb, C., Gomez-Rivas, E., Bons, P.D. & Blum, P., 2013. Evaluation of sampling methods for fracture network characterization using outcrops, *AAPG Bull.*, **97**(9), 1545–1566.

APPENDIX : NUMERICAL UPSCALING PROCEDURE

Following Rubino *et al*. (2014), we represent fractures as highly compliant and permeable heterogeneities embedded in a stiffer porous background, and we model the behavior of fractured media in the framework of Biot's (1941) theory of quasi-static poroelasticity. Fluid-pressure communication between fractures and their embedding background as well as within connected fractures can take place, which allows to account for the effects produced by the two manifestations of WIFF.

In order to estimate the effective seismic properties of fractured rocks, we employ a numerical upscaling procedure based on the application of three oscillatory relaxation tests on a square sample that is representative of the formation of interest (Rubino *et al*. 2016). First, we apply homogeneous oscillatory vertical displacements on the top and bottom boundaries of the representative sample, while it is not allowed to have horizontal displacements on the lateral boundaries. Moreover, we do not allow the fluid to flow into the sample or out of it. Next, a second test similar to the previous one is applied, but the normal displacements are applied on the lateral boundaries. Finally, a third test consisting of a simple shear is applied to the probed sample.

The solid and relative fluid displacements in response to the three tests are obtained by numerically solving, under corresponding boundary conditions, the Biot's (1941) quasistatic poroelastic equations in the space-frequency domain:

$$\nabla \cdot \boldsymbol{\sigma} = 0, \tag{A1}$$

$$i\omega \frac{\eta}{\kappa} \mathbf{w} = -\nabla p_f, \tag{A2}$$

where $\boldsymbol{\sigma}$ is the total stress tensor, p_f is the fluid pressure, $\mathbf{w}$ is the average relative fluid displacement, η is the shear viscosity of the pore fluid, κ is the rock permeability and ω is the angular frequency.

Next, for each test, we compute the volume averages of the stress and strain components, which are needed for performing the upscaling:

$$\langle \varepsilon_{ij}^k \rangle = \frac{1}{V} \int_\Omega \varepsilon_{ij}^k \mathrm{d}V, \tag{A3}$$

$$\langle \sigma_{ij}^k \rangle = \frac{1}{V} \int_\Omega \sigma_{ij}^k \mathrm{d}V, \tag{A4}$$

where $\boldsymbol{\varepsilon}$ is the strain tensor, Ω is the domain of volume V that represents the probed sample and $k = 1,2,3$ denotes the kth oscillatory test described above.

Assuming that the average responses of the probed sample can be represented by an equivalent homogeneous anisotropic viscoelastic solid, the average strain and stress components are then connected through a complex-valued frequency-dependent equivalent Voigt stiffness matrix **C**:

$$\begin{pmatrix} \langle \sigma_{11}^k \rangle \\ \langle \sigma_{22}^k \rangle \\ \langle \sigma_{12}^k \rangle \end{pmatrix} = \begin{pmatrix} c_{11} & c_{12} & c_{16} \\ c_{12} & c_{22} & c_{26} \\ c_{16} & c_{26} & c_{66} \end{pmatrix} \begin{pmatrix} \langle \varepsilon_{11}^k \rangle \\ \langle \varepsilon_{22}^k \rangle \\ \langle 2\varepsilon_{12}^k \rangle \end{pmatrix}. \tag{A5}$$

Please note that the stiffness coefficients in eq. (A5) are similar to those of the corresponding 3-D samples under the plane strain condition.

Eq. (A5) holds for the three oscillatory tests described above. We therefore establish nine equations, and the six unknown stiffness coefficients are obtained by using a classic least-squares algorithm. The reader is referred to the work of Rubino *et al*. (2016) for the details of the numerical upscaling procedure.